

EXTREMELY EFFICIENT AND ULTRAFAST:
ELECTRONS, HOLES, AND THEIR INTERACTIONS IN THE
CARBON NANOTUBE PN JUNCTION

A Dissertation

Presented to the Faculty of the Graduate School
of Cornell University

In Partial Fulfillment of the Requirements for the Degree of
Doctor of Philosophy

by

Nathaniel Monroe Gabor

May 2012

© 2012 Nathaniel Monroe Gabor

EXTREMELY EFFICIENT AND ULTRAFAST:
ELECTRONS, HOLES, AND THEIR INTERACTIONS IN THE
CARBON NANOTUBE PN JUNCTION

Nathaniel Monroe Gabor, Ph. D.

Cornell University 2012

The electronic properties of charge carriers in carbon nanotubes exhibit striking similarities to relativistic elementary particles. A remarkable prediction of relativistic quantum mechanics is the ability of particle-antiparticle pairs to be created and annihilated when interacting with other high-energy particles. In this thesis, I discuss optoelectronic experiments that probe the extremely efficient generation of electron-hole pairs and the (ultra-) fast transit of these electrons and holes through nanotube PN junction photodiodes. Spatially, spectrally, and temporally resolved photocurrent measurements suggest that the generation of multiple electron-hole pairs from a single high energy carrier is extremely efficient, and that electrons and holes may undergo electron-hole pair annihilation as they transit the junction on sub-picosecond time scales. These processes, analogous to relativistic particle-antiparticle creation and annihilation, set new boundaries for the performance limits of nanoscale optoelectronic devices.

BIOGRAPHICAL SKETCH

Nathaniel Gabor, born in Jeanette, Pennsylvania on the third wintery morning in 1981, built his first working robot of Lego blocks later that decade. Satisfied with his engineering skills yet driven by curiosity, he moved on to more artistic endeavors: pen and ink drawing, pottery, sculpting and painting soldiers, monsters, and other fantastic creatures. Such obsessions left little time for academics. Little did Nathaniel realize that these obsessions - building, sculpting and curiosity - would motivate him without end.

In high school, Nathaniel spent much of his time toiling away creating a fantastic gaming realm with his younger brother Jared and a group of like-minded misfits. Suddenly, one summer afternoon in 1997, like a hobbit being intruded upon by a wandering wizard, there was a knock on his door. There at the door stood Angela, with whom Nathaniel would partake in many adventures and would later marry in Ithaca, New York while attending graduate school at Cornell University.

At Penn State University and later at Cornell, Nathaniel's passion for building, sculpting and curiosity would eventually evolve into a similarly deep passion for equations, phenomenological descriptions, and physical constants. He had become a physicist, yet had held on vehemently to all the things he loved – art, games, yoga, family and friends. Nathaniel defended his graduate thesis in the Fall of 2010 and, nearly one and a half years later, finished the written portion of his thesis while attending MIT as a postdoctoral researcher. As with most things in Nathaniel's life, clerical responsibilities were never as strong a force as curiosity.

To family, friends, and above all, Angela

ACKNOWLEDGMENTS

Doing science is like cooking for friends. You only share the recipes that really worked, and you don't mention the other 90% that failed, but that you ate anyway. This thesis is the cookbook of some of the recipes that worked, and only here do I get to mention the many, many friends.

First, I must thank Paul McEuen, my advisor, my colleague, and a dear friend. Only when I left Cornell did I realize what I had left. As many of his students know, life and work at Cornell was wonderful in a large part because of Paul's advising. His intellect is as sharp as his heart is big, and it truly was a long strange trip. Thank you.

At Cornell, I met some of the best friends of my life, and some of the most impressive colleagues. In the facilities at Cornell and the research groups of Bob Buhrman, Itai Cohen, Seamus Davis, Veit Elser, Alex Gaeta, Michal Lipson, Jiwoong Park, Dan Ralph, Kyle Shen, and of course Paul McEuen, I found many talented scientists that were always willing to share ideas, inspirations, and critical thoughts. These groups and their members define the congeniality of Cornell and, as I have found after my time at Cornell, this congenial environment is the envy of many of the most elite departments. Of all these individuals, many names stick out: Jonathan, Arthur, Melina, Arend, Josh, Samantha, Simon, John, Matt, Sharon, Duane, Andy, Isaac, Ken, Shahal, Jun, Patrycja, Luke, Marcus, Rob, Jon, Scott, Lisa, Sami, Vera, Vlad, Xiaodong, Xin, Xinjian, Yaqiong, Yoshi, Zhaohui and many others beside.

In Ithaca, I managed to plant deep roots and along with those roots came many incredible friends. My artwork and creativity were strongly supported by many people and with them I have left much of my work: Carol, David, Carrey, Mimi, Steve, and many others. Aside from artwork, there was another art that I practiced in Ithaca - yoga. In this and many respects, Steven Valloney was a wonderful inspiration, an incredible guide and a great friend. As I continue in this aspect of my life, I am extremely grateful for Steven and many others in Ithaca: Anne, Pete, Norinne, Nicole, Kate, Ben and everyone at Sunrise.

Finally, I must thank my family: Mom, Dad, Courtney, Dan, and Jared. You have all contributed to anything to which I have amounted, for better or worse, and I hope that I have proven myself a good son and brother throughout this life. And Angela, ever since that fateful day when you knocked on my door, I knew something was very special about you, thank you. Thank you for all the time that we've shared peeling back the layers only to find more beautiful expressions.

“Listen, there’s a hell of a good universe next door: Let’s go.”

- e.e. cummings

TABLE OF CONTENTS

Biographical Sketch	iii
Acknowledgements	v
Chapter 1: Introduction and Background	
1.1 Introduction: Light-Matter Interactions at the Nanoscale	1
1.2 Semiconductor Optoelectronics: The PN Junction	3
1.3 Carbon Nanotube Field Effect Devices and the Nanotube PN Junction	5
1.4 Transport in One Dimension: Ballistic vs. Diffusive	9
1.5 Optical Excitation in One Dimension: Density of States	12
1.6 Summary and Outline	15
Chapter 2: Theory of Carbon Nanotube Band Structure	
2.1 Introduction	18
2.2 Nanotubes Formed of Rolled Graphene	18
2.3 Band Structure of Graphene	20
2.4 Electronic Wave Functions in a Graphene Cylinder	23
2.5 Band Structure of Semiconducting Nanotubes	26
2.6 Carrier Interactions in Nanotubes	29
2.7 Carrier Interactions: Electron-Hole Pair Creation	30
2.8 Carrier Interactions: Electron-Hole Pair Annihilation	33
2.9 Conclusion	36
Chapter 3: Instrumentation: Low Temperature Scanning Photocurrent Microscope	
3.1 Introduction	37
3.2 The Scanning Photocurrent Spectroscopy Microscope	37
3.3 Combining Low Temperature Electronics and Optics	40
3.4 Spatially Resolved Laser Excitation	42
3.5 Spectrally Resolved Supercontinuum Excitation	47
3.6 Temporally Resolved Ultrafast Laser Excitation	49
3.7 Conclusion	51

Chapter 4: Electronic Transport in the Nanotube PN Junction

4.1	Introduction	52
4.2	Device Fabrication	53
4.3	Device Characteristics and Gate Dependence	55
4.4	Forward Bias: Temperature Dependence Measurements	58
4.5	Model: Thermal Activation Across a One-dimensional Barrier	60
4.6	Reverse Bias and Diode Breakdown	65
4.7	Conclusion	68

Chapter 5: Multiple Electron-Hole Pair Generation in Nanotube PN junctions

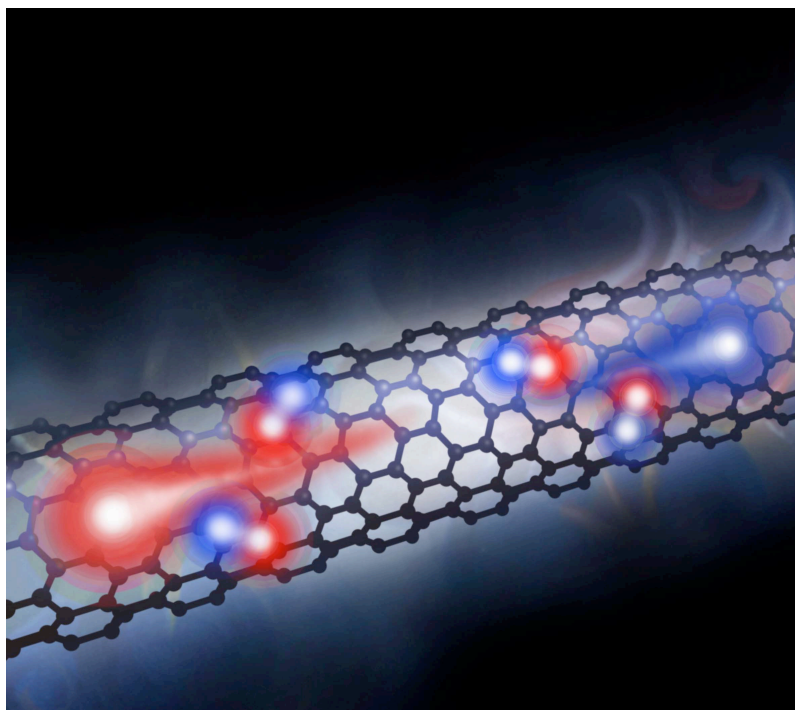
5.1	Introduction	70
5.2	Scanning Photocurrent Microscopy and I - V_{SD} Characteristics	71
5.3	Optoelectronic I - V_{SD} Characteristics: Photon Energy and Diameter Dependence	73
5.4	Photocurrent Spectroscopy and Temperature Dependence	76
5.5	Model: Extremely Efficient Impact Excitation	79
5.6	Spatial Dependence of Photocurrent in the PN Junction	81
5.7	Discussion and Comparison to Theoretical and Experimental Work	84
5.8	Conclusion	86

Chapter 6: The Escape of Electrons and Holes From the Nanotube PN junction

6.1	Introduction	88
6.2	Measuring Photocurrent at Ultrafast Time Scales	89
6.3	Single Pulse Photocurrent: Sublinear Behavior	91
6.4	Double Pulse Photocurrent: V_{SD} Dependence	91
6.5	Model: The Escape Time of Electrons and Holes From the PN Junction	94
6.6	Double Pulse Photocurrent: Photon Energy Dependence	98
6.7	Double Pulse Photocurrent: Reverse Bias	98
6.8	Conclusion	100

Chapter 7: Conclusion

7.1	The PN Junction Then and Now	101
-----	------------------------------	-----



CHAPTER 1

INTRODUCTION AND BACKGROUND

1.1 Introduction: Light-Matter Interactions at the Nanoscale

From Maxwell's unification of the electric and magnetic fields in matter to Einstein's description of the photoelectric effect, the interactions of light and matter have driven the curiosity of generations of scientists. The investigation of light-matter interactions continues to intrigue even in the present day as new materials are being discovered and experimental techniques are advancing. An important focus of modern investigations is nanoscale technology, technology at the length scale that represents the limit of our current ability to manipulate and develop complex structures. When electrons in a material are confined to dimensions of several nanometers (smaller than their Fermi wavelength), the classical physical descriptions no longer apply. At this size scale, the fundamental electronic excitations become quantized and the interactions of light and matter result in exotic physical behavior.

There are two complex nanotechnologies in which light-matter interactions are reasonably well understood: semiconductor based optoelectronics and the biological infrastructure of photosynthesis. As shown in Figure 1.1, these technologies are based on very different functional elements. The basic building block of many semiconductor electronics is the silicon crystal (Figure 1.1a), a periodic array of Si atoms whose electrons are extended states described by electronic bands. On the other hand, the building block of biological photosynthesis is the chlorophyll molecule (Figure 1.1b), an organic molecule whose electrons are tightly confined and form quantized states. At the conceptual boundary between semiconductor crystal and carbon-based molecule sits the carbon nanotube (NT). Composed of a periodic array of carbon atoms with physical dimensions comparable to many biological molecules, the NT has aspects of both semiconductor and biological nanomaterials. Due to these combined aspects, light-matter interactions in NTs have been the subject of tremendous theoretical and

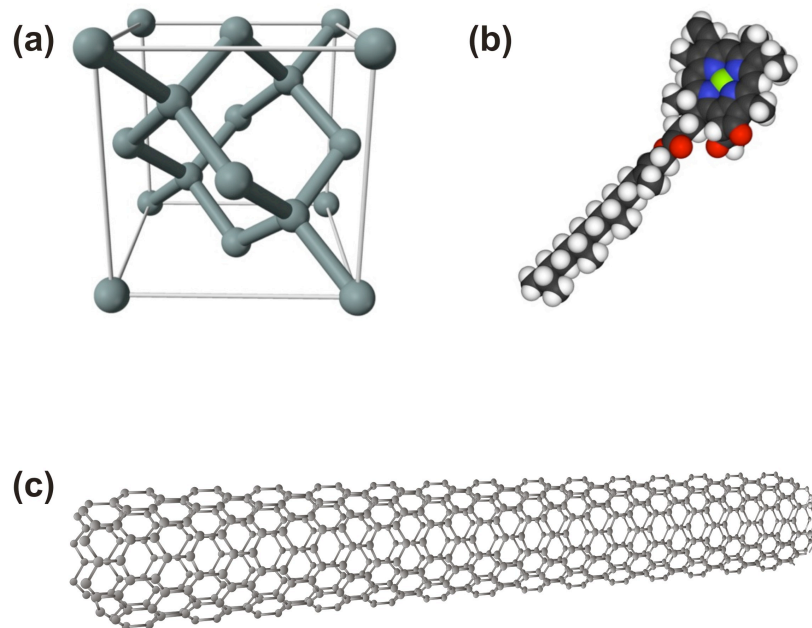


Figure 1.1. Nanotechnologies for the investigation of light-matter interactions. **(a)** The basic crystal structure of bulk silicon, the basis of semiconductor electronics and optoelectronics. The electrons in bulk crystals are extended states defined by the material's band structure. **(b)** The fundamental molecule for biological photosynthesis, chlorophyll a. The electrons in molecules are tightly confined and form a discrete energy spectrum. **(c)** Carbon nanotubes combine aspects of both the semiconductor and biological nanotechnologies. The electrons in nanotubes are extended states in one dimension, but tightly confined in the remaining two dimensions.

experimental work. In this chapter, we first introduce an experimental infrastructure for investigating light-matter interactions and we present some of the interesting properties of NTs. In the remainder of this thesis we present experiments that explore light-matter interactions in NT devices and demonstrate some of the exotic behavior that results from the NT's unique aspects.

1.2 Semiconductor Optoelectronics: The PN Junction

There are numerous approaches to studying light-matter interactions in a novel material such as NTs. As physicists and nanotechnologists, our experimental approach takes inspiration from the compilation of knowledge based on over half a century of semiconductor technology. As we will discuss at the end of this chapter, we aim to integrate NTs into semiconductor photodiodes and study the optoelectronic characteristics. Before discussing this, however, it is important to understand the basic working principles of a key semiconductor device for light-matter investigations: the PN junction.

Figure 1.2a shows the first patent of a PN junction by R.S. Ohl at Bell Telephone Labs (1941). Ohl's "light sensitive device" combines two semiconductor silicon crystals, one doped with electron donors (p-type material) and the other with electron acceptors (n-type material) (Ohl 1941, Sze 1981). By placing the two materials together, Ohl discovered that the electrons and holes at the interface are redistributed to form a built-in electric field. Because the PN junction is composed of semiconducting materials, the minimum energy required to excite an electron from the valence band to the conduction band is the band gap energy E_{GAP} . The resulting electronic potential energy landscape and schematic device characteristics are shown in figure 1.2b. In the absence of light, when a positive voltage is applied across the device, the potential energy barrier at the PN junction is reduced, effectively opening the floodgate for electrons and holes and resulting in exponential turn-on in forward bias. When a negative voltage is applied the potential barrier is increased, and no current passes through the device.

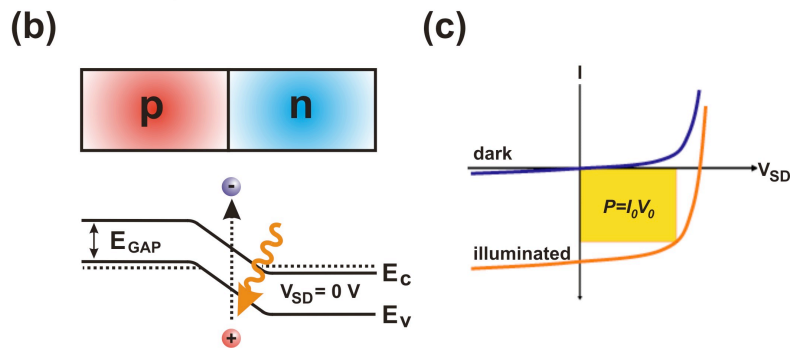
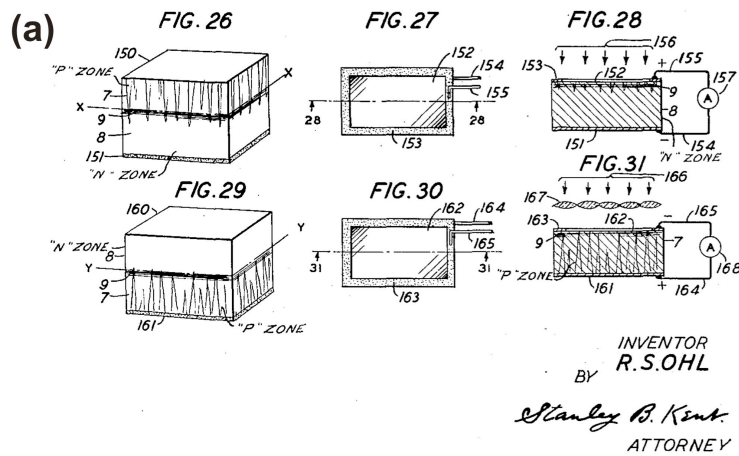


Figure 1.2. The semiconductor PN junction. **(a)** R.S. Ohl's original patent of a "light sensitive device". A "P" zone (positively doped Si semiconductor) and an "N" zone (negatively doped semiconductor) were combined to form a PN junction. **(b)** Schematic potential energy diagram for electrons in a PN junction showing the potential energy barrier (or built-in electric field). An incident photon excites an electron-hole pair in the junction. The electron-hole pair is separated and collected at the device contacts. **(c)** Typical current-voltage characteristics for a conventional PN junction.

If a photon whose energy exceeds the band gap energy is incident on the PN junction, it creates an electron-hole pair that is separated by the electric field and collected at the contacts. This leads to additional current that offsets the dark I - V characteristic. In forward bias, the amount of optical power converted to electrical power generated in the device, $P = I_0 V_0$, is the power conversion efficiency. This is the basic operating principle of solar cell devices used for energy harvesting. In reverse bias, the built-in field may become so strong that electrons and holes are accelerated to high kinetic energies and undergo avalanche multiplication. This is the operating regime of avalanche photodiodes. As can be seen, the PN junction is a vital electronic and optoelectronic element in modern electronics, but also provides an excellent experimental platform to study light-matter interactions in novel semiconductor materials such as NTs.

1.3 Carbon Nanotube Field Effect Devices and the Nanotube PN Junction

Carbon nanotube field effect transistors (FETs) have served as the workhorse for quantum electronic, (Tans, Devoret et al. 1998, review McEuen et al. 1998, Bockrath et al. 1999, review Dekker et al. 1999) as well as chemical and biological sensing (Kong et al. 2000, Li et al. 2003, Snow et al. 2005, Larrimore et al. 2006, Zhou et al. 2007) measurements in NTs. Of interest to applied technologies, semiconducting NT field effect devices have been fabricated with excellent properties that push fundamental transport limits (Zhou thesis 2008, Rosenblatt et al. 2007, Lu et al. 2004, Javey et al. 2002). In this section, we briefly review the operating principle of NT field effect devices (for more detailed descriptions see, for example, Rosenblatt thesis 2006), as this will form the basis of our PN junction device.

Figure 1.3a shows the conventional nanotube FET geometry. An insulating layer of silicon dioxide separates a conducting gate electrode (GATE) from an individual semiconducting nanotube. The NT forms the channel through which electrons and holes may travel. A voltage applied to the conducting gate, which is capacitively coupled to the NT channel, establishes an electric field that can alter the local electrostatic environment of the NT.

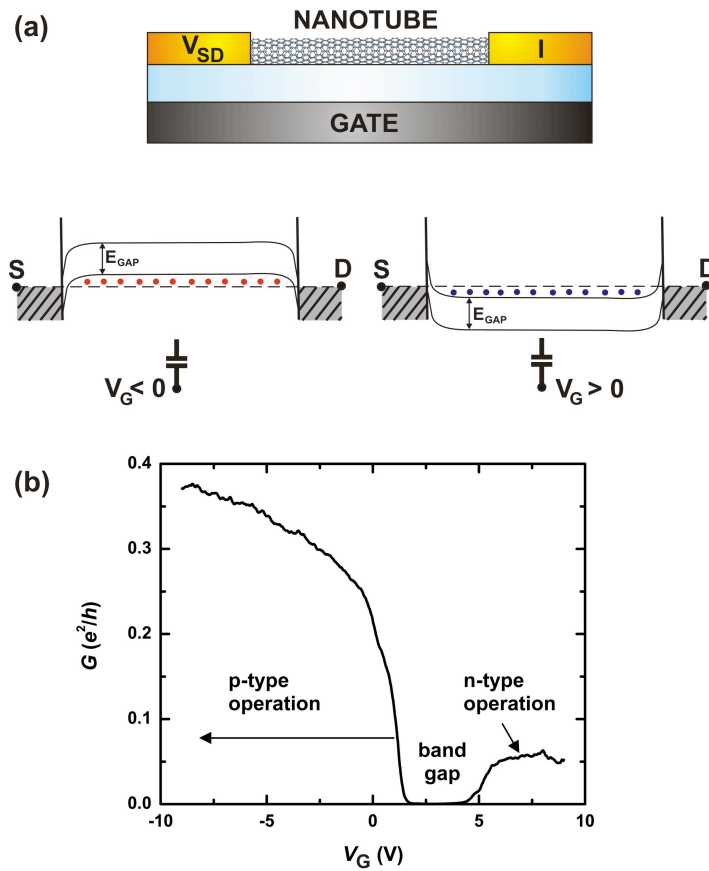


Figure 1.3. The nanotube field effect transistor (FET). **(a)** Schematic diagram of the NT FET and the potential energy landscape for p-type (left) and n-type (right) operation (described in text). The semiconducting NT is contacted between source (S) and drain (D) electrodes and has band gap energy E_{GAP} . **(b)** Conductance G vs. gate voltage V_G characteristics for a typical semiconducting NT device. When $V_G < 0$ ($V_G > 0$) the device operates as a p-type (n-type) conductor. Between p- and n- type conduction, the device shows an insulating "off" state corresponding to the band gap of the NT.

In Figure 1.3a, we show how the electron potential energy landscape is affected when a voltage is applied to the gate electrode. When the gate voltage V_G is negative, positive charges (holes) accumulate in the NT channel in order to reach electrostatic equilibrium, pushing the electron Fermi level below the valence band edge. Applying a voltage between the source (S) and drain (D) electrode leads to a conductive "on" state and the device is a p-type conductor. Conversely, when the gate voltage is positive, electrons accumulate in the NT channel resulting in n-type "on" conductance. Since a semiconducting NT has a typical band gap of ~ 0.5 eV, there is a significant range of applied gate voltages in which the Fermi level lies within the band gap. When the Fermi level is in the center of the gap, both the valence and the conduction states are filled (at $T = 0$) resulting in a non-conducting or insulating "off" state.

The conductance G vs. gate voltage V_G of a typical semiconducting device (Figure 1.3b) shows p-type operation, n-type operation, and an insulating "off" state. In real NT devices, the n-type conductance is generally much less than the p-type conductance due to large tunneling barriers for electrons at the p-type contacts (typically gold or palladium). Also, excess positive charge on the NT due to fabrication processing results in intrinsic p-type behavior leading to the offset of the insulating regime in the G - V_G characteristics. Significant experimental work has determined the ideal materials and processing that improve NT device performance and opened the door to applications in high frequency and high performance electronics (see introductory references).

The above description shows that NTs in a single gate device operate as either p-type or n-type conductors. An interesting question then arises: can we fabricate a field effect device that allows us to make a junction between p- and n-type regions on the same nanotube? In Figure 1.4, we show the geometry and potential energy landscape of a nanotube field effect PN junction. In this geometry, two independent gates V_1 and V_2 allow selective electrostatic doping of the NT channel. Just as in Ohl's PN junction, a built-in electric field forms between p- and n- regions when we apply voltages of opposite polarity on these gates. The resultant device, first proposed and fabricated by Lee et al (2004), is a PN junction in which the fundamental operating element

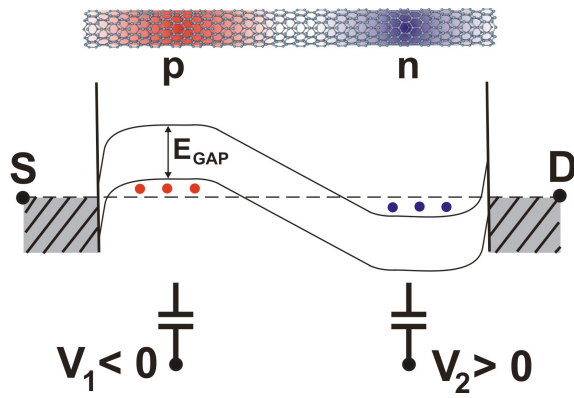


Figure 1.4. The semiconducting nanotube PN junction. By locally gating an individual NT along its length, a p-type and n-type region can be established. The PN junction at the boundary between p- and n- regions leads to a built-in electric field.

is a one-dimensional quantum wire formed of a semiconducting nanotube. In Chapter 4, we describe the fabrication of a NT PN junction and present measurements electronic and optoelectronic measurements of this novel device.

1.4 Transport in One Dimension: Ballistic vs. Diffusive

Unlike Ohl's PN junction, the NT PN junction incorporates a one-dimensional (1D) electronic channel. Therefore, in order to fully understand the optoelectronic device behavior of the NT PN junction, it is important to understand 1D electronic and 1D optical properties. We begin here with a discussion of 1D transport and follow with a discussion of 1D optical absorption in Section 1.5. One-dimensional nanoscale structures, such as NTs, are often of comparable dimensions to the scattering length of charge carriers. When no scattering is present, NTs operate as ballistic electronic conductors. These ballistic devices act as electron waveguides and the transport behavior can be described using the Landauer-Buttiker formalism (review Datta 1995). In the presence of scattering, however, the NT operates in the diffusive transport regime and can be described by a semi-classical model (Zhou thesis 2008, Zhou 2005, Datta 1995). In this section we present simple expressions that describe the device conductance in these two regimes. Understanding the ballistic and diffusive transport regimes will become important in understanding the experimental results of Chapters 4, 5 and 6.

In the absence of scattering, conduction through a 1D channel is ballistic. To calculate the current that will pass through a ballistic conductor, it is convenient to calculate the imbalance of left-moving and right-moving electrons in the device. When no applied electric field is present, the right- and left- moving electrons are equal and no net current flows. However, applying an electric field breaks this balance, resulting in a net flow of charge in one direction. Since the electrons do not scatter within the channel, the net current can be calculated from the charge imbalance at the electrodes:

$$I = (n_R - n_L)e v = \int \left(\frac{dn}{dE} (f_R(E) - f_L(E)) \right) e \frac{1}{\hbar} \frac{dE}{dk} dE. \quad (1.1)$$

Here, n_R and n_L are the number of right- and left- moving electrons in the device, $v = 1/\hbar(dE/dk)$ is the velocity of these electrons determined by the band structure $E(k)$, dn/dE is the density of states per unit length of the channel, and f_R and f_L are the Fermi distributions in the right and left electrodes. In Equation (1.1), dn/dE can be re-written as $(dn/dk) / dE/dk = 1/\pi (dE/dk)$. This leads to an expression for the current

$$I = \frac{2e}{h} \int (f_R(E) - f_L(E)) dE \quad (1.2)$$

that can be further simplified by considering that the integrated difference in the relative electron distribution is directly related to the applied voltage eV . This results in a very simple expression for the conductance G :

$$G = \frac{I}{V} = \frac{2e^2}{h} \quad (1.3)$$

where $2e^2/h$ is the well-known quantum of conductance (experimentally verified by Van Wees et al. 1998, Wharam et al. 1988).

When electrons in a ballistic conductor encounter a potential barrier in the channel, they will be reflected and transmitted just as in a 1D waveguide. Equation (1.2) can be generalized by including a transmission coefficient $\mathfrak{S}(E,V)$ that depends on the energy E and the applied voltage V . The current can then be calculated in a similar way to Equation (1.2):

$$I = \frac{2e}{h} \int \mathfrak{S}(E,V) (f_R(E) - f_L(E)) dE \quad (1.4)$$

In Chapter 4, we will revisit Equation (1.4) to understand ballistic transport behavior in NTs.

In the presence of random carrier scattering, we can calculate the current through the device in a similar fashion to the ballistic case using the semi-classical relaxation time approach. To do this, we replace the distribution functions f_R and f_L at the two ends of the device with a modified distribution g that is a function of position and time and must be integrated over the device length. In the presence of an applied electric field \mathbf{E} , we must integrate the balance of right- and left- moving carriers in the presence of many scattering events. To quantify the scattering events, we first assume that any scattering event takes the electron distribution away from the initial Fermi distribution. We then introduce a relaxation time τ that represents the amount of time for the modified distribution to relax back to the initial distribution. The modified distribution then takes the form $g = e\tau(k)\mathbf{E}v(k)$ where $v(k)$ is the velocity and $\tau(k)$ is the relaxation time. The device current can then be written as

$$I = \frac{2e^2}{h} \tau(k_F) \mathbf{E} v(k_F) \quad (1.5)$$

where the relaxation time and the velocity have been evaluated at the Fermi level. For a voltage V applied over a device length L , the electric field is $\mathbf{E} = V/L$ and the conductance G can be written as

$$G = \frac{2e^2}{h} \frac{\tau(k_F) v(k_F)}{L} = \frac{2e^2}{h} \frac{L_{MFP}}{L} \quad (1.6)$$

where $L_{MFP} = \tau(k_F) v(k_F)$ is the mean free path of the electron in the presence of the relevant scattering process and, again, $2e^2/h$ is the quantum of conductance.

While Equation (1.3) represents the perfectly transparent ballistic device, Equation (1.6) represents current through a one-dimensional device in the presence of scattering. In either case in NTs, the 1D conducting channels come in degenerate pairs due to the sub-lattice degeneracy of graphene and resulting band structure of NTs (described in Chapter 2). Therefore, in nanotubes, Equations (1.3) and (1.6) take the forms

$$G_{NT} = \frac{I}{V} = \frac{4e^2}{h} \quad (\text{ballistic}) \quad (1.7)$$

$$G_{NT} = \frac{4e^2}{h} \frac{L_{MFP}}{L} \quad (\text{scattering}). \quad (1.8)$$

Depending on the particular experimental regime, both ballistic and diffusive transport has been observed in NTs. As shown in Figure 1.5, when the device length L is less than the mean scattering length of a given scattering mechanism, ballistic transport results. When the device length is long compared to the scattering length, diffusive transport results. In NTs, scattering of electrons and holes occurs at many length scales and through many processes. One particular scattering process in NTs, electron-phonon scattering, has been well studied experimentally and theoretically (Zhou et al. 2005, Park et al. 2004, Yao et al. 2000, Hertel et al. 2000, Perebeinos et al. 2005, review Avouris et al. 2007) and scattering lengths have been determined for high energy optical phonons ($L_{OP} \sim 30$ nm) and low energy phonons ($L_{AC} > 1$ micron). For devices shorter than these mean free paths, ballistic transport has been observed even at room temperature (Javey et al. 2004).

1.5 Optical Excitation in One Dimension: Density of States

In addition to electronic transport, we must also understand how light interacts with a one-dimensional nanotube. In general, when a photon is incident on a semiconductor, it may generate an electron-hole pair. The probability of photon absorption depends on the number density of available electronic states (DOS). Since the NT is a 1D material, the DOS will differ dramatically from the three-dimensional (or bulk) DOS. In this section, we derive and present an expression for the DOS in NTs (Dresselhaus et al. 2001). As we will see, understanding the optical absorption of photons into electronic states will be important in understanding the experiments presented in Chapters 5 and 6.

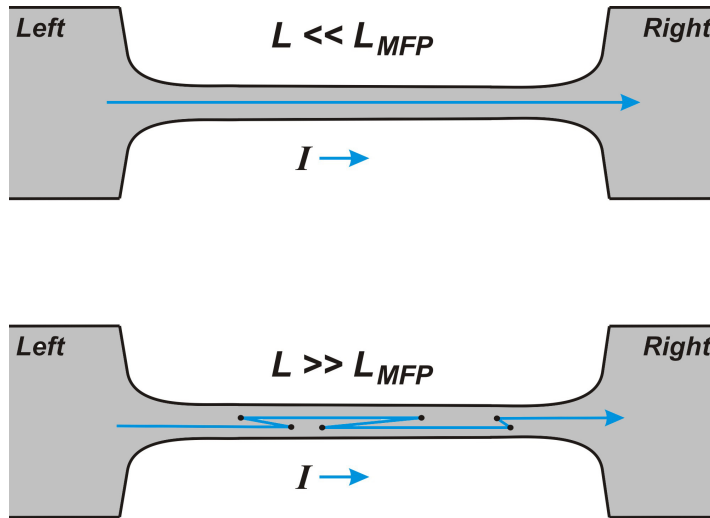


Figure 1.5. Ballistic vs. Diffusive transport in one-dimensional electronics. **(top)** In ballistic transport, the device length L is much less than the mean free path of electrons L_{MFP} in the presence of a given scattering process. Electrons in a ballistic conductor travel as waves and can be described by the Landauer-Buttiker formalism. When a voltage is applied, the number of right-moving electrons exceeds the number of left-moving electrons, leading to a current I . **(bottom)** In diffusive transport, the device length is much longer than the scattering length L_{MFP} . In 1D, this can be described using a semi-classical model.

As we will discuss in detail in Chapter 2, the energy dispersion relation of nanotubes is derived by simply slicing the two-dimensional graphene energy dispersion with a line in crystal momentum- or k -space offset by some vector k_0 . This results in a 1D energy dispersion of the form

$$\varepsilon(k_{\parallel}) = \pm \hbar v_F \sqrt{k_{\parallel}^2 + k_0^2} \quad (1.9)$$

where the Fermi velocity is given by $v_F = \sqrt{3}ta_{C-C}/2\hbar$ and the electrons are confined to one direction $\pm x$ parallel to the length of the NT. In the expression for the Fermi velocity, a_{C-C} is the carbon-carbon bond length and t is the tight-binding overlap integral between carbon atoms. From this geometric derivation, the relationship between the wave vector offset k_0 and the band gap energy can be expressed as

$$E_{GAP} = 2\hbar v_F k_0 = 2ta_{C-C}/d \quad (1.10)$$

where the last step is valid for semiconducting devices of diameter d .

With this simple expression for the band dispersion in NTs, we can now calculate the 1D density of states. The density of states in a one-dimensional NT of length L is given by

$$\frac{dN}{dE} = 2 \cdot \frac{L}{2\pi} \cdot \frac{4}{|dE/dk|} \quad (1.11)$$

The factor of 2 arises from the spin up and spin down contributions to the density of states. The factor of 4 originates from the contribution of right- and left- moving carriers and the sub-lattice degeneracy in graphene. Using the expressions above for the energy dispersion in NTs, we can determine dE/dk

$$\left| \frac{dE}{dk} \right| = \frac{\hbar v_F k}{\sqrt{k_{\parallel}^2 + k_0^2}} = \hbar v_F \frac{\sqrt{\varepsilon^2 - (E_{GAP}/2)^2}}{\varepsilon} \quad (1.12)$$

We define $n = N/L$ as the linear electron density and combine the above expressions to get the number density of states (DOS) in the NT:

$$\frac{dn}{dE} = \frac{8}{3\pi a_{C-C}} \frac{\epsilon}{\sqrt{\epsilon^2 - (E_{GAP}/2)^2}} \quad (1.13)$$

This expression results in the well-known van Hove singularities: when $\epsilon = \pm(E_{GAP}/2)$, the DOS goes to infinity. While the above expression only considers the lowest subband, NTs have many higher energy subbands that also lead to singularities in the DOS. Figure 1.6 shows an example of the DOS in a semiconducting NT as a function of the carrier energy. In the example of Figure 1.6, singularities appear at the band gap edge $\epsilon = \pm(E_{GAP}/2)$ (where $\Delta\epsilon = E_{GAP}$) as well as at the second subband edge that occurs at twice this energy $\epsilon = \pm E_{GAP}$ (where $\Delta\epsilon = 2E_{GAP}$).

Singularities in the NT DOS increase the probability of photon absorption leading to the generation of electron-hole pairs. In order to excite the lowest energy free electron and hole, the total photon energy E_{PH} must equal the band gap $E_{PH} = E_{GAP}$, while second subband electron-hole pairs can be excited if $E_{PH} = 2E_{GAP}$. Numerous optical measurements have accessed these energies in NTs and much is known about the fundamental optical excitations and their relaxation (review Jorio, Dresselhaus et al. 2008). While the DOS description captures the basic physics of photon absorption into single electron states, bound states called excitons are also quite important (Kane and Mele 2003, Kane and Mele 2004, Spataru et al. 2004, Wang et al. 2005)). The relative importance of, and interactions between, bound excitons and free electrons and holes are still not understood, particularly when optics is combined with NT electronic devices.

1.6 Summary and Outline

Experiments presented in this thesis explore the overlap between electronic and optical properties in NTs. In this chapter, we presented some of the interesting historical background

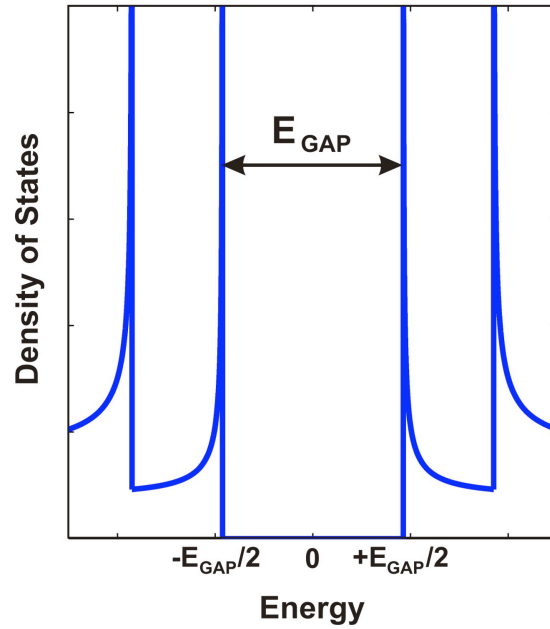


Figure 1.6. Nanotube one-dimensional density of states (DOS). The DOS shows singular behavior at several energies, each corresponding to a different subband in the nanotube band structure. In a semiconducting NT, the lowest energy van Hove singularities occur at the band gap energy, while the second singularity occurs at twice this energy. Generation of an electron-hole pair by absorption of a photon depends directly on the DOS. An incident photon must have energy that is equal to or greater than the band gap energy in order to be absorbed.

and basic operation of one of technology's most important devices: the semiconducting PN junction. We then proposed a field effect PN junction composed of an individual carbon nanotube and discussed the basic physics of electron transport and optical absorption in one dimension. In Chapter 2, we will discuss the NT band structure and carrier-carrier interactions, emphasizing the ideas required to understand later experimental results. Chapter 3 gives a full description of the experimental tools used to conduct these measurements. Following these introductory chapters, the remainder of the thesis presents experimental results. Chapter 4 focuses on fabrication and low temperature electronic measurements of the NT PN junction, while Chapter 5 and Chapter 6 discuss optoelectronic measurements. As will be seen, these measurements demonstrate some of the unique properties of NTs, but also reveal very surprising optoelectronic behavior.

CHAPTER 2

THEORY: BAND STRUCTURE AND INTERACTIONS OF CARRIERS IN CARBON NANOTUBES

2.1 Introduction

While vast, theoretical and experimental work on carbon nanotubes (NTs) has not yet developed a complete description of strongly interacting carriers, particularly at carrier energies comparable to the band gap. In this chapter, we discuss the theoretical basis for two processes that result from strong carrier interactions at high energies: particle-antiparticle creation (or impact ionization) (Kane and Mele 2003, Perebeinos et al. 2006) and particle-antiparticle annihilation (Auger recombination) (Kinder et al. 2008, Valkunas et al. 2006, Wang et al. 2006). At the end of this chapter, we discuss these processes in carbon nanotubes and highlight some of the key aspects.

Before developing a theoretical discussion of carrier interactions in NTs, we begin this chapter by briefly highlighting the electronic band structure of nanotubes, detailed reviews of which can be readily found (Dresselhaus 2001, McEuen 2000, White and Mintmire 1998). Of particular interest, following Ilani et al. (2010), we present a very intuitive geometric description of this band structure. Having established this simplified description, we then discuss the particle-antiparticle (electron-hole pair) creation and annihilation processes. Discussion of electronic band structure and carrier interactions lays the theoretical groundwork required to understand the experimental results presented in Chapters 4, 5 and 6.

2.2 Nanotubes Formed of Rolled Graphene

Carbon nanotubes can be visualized as a single layer of graphene that has been rolled into a tube (Figure 2.1). Since the graphene lattice has an underlying six-fold symmetric atomic structure, rolling graphene into a tube results in a wide variety of atomically structured NTs.

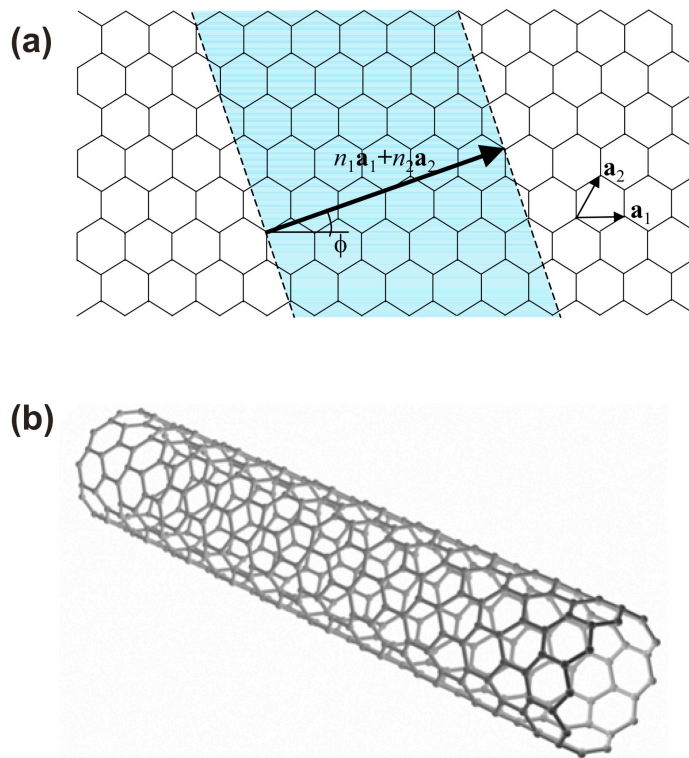


Figure 2.1. Schematic diagram of the graphene lattice and a rolled nanotube. **(a)** The nanotube is formed of rolled graphene by matching the tail to the tip of the wrapping vector $n_1\mathbf{a}_1 + n_2\mathbf{a}_2$. The nanotube **(b)** can then be assigned an index (n_1, n_2) or $[d, \phi]$ that fully describes the nanotube structure. The relationship of the six-fold symmetric graphene to the geometry of the tube determines the physical properties. Images adapted from Minot 2004 and L. Larrimore 2008.

Each NT structure (or species) can be distinguished by the way in which atoms of the former graphene lattice meet to form the rolled NT. While the resulting NT maintains a well-ordered atomic structure, the relationship between the underlying six-fold symmetry and the tube geometry become crucial in understanding the NT properties.

To map the six-fold atomic symmetry of the graphene lattice into a tube, it is convenient to define a wrapping vector (Figure 2.1a). The wrapping vector traces out the circumference of the NT and fully describes the NT atomic structure. In the example of Figure 2.1a, the shaded area of graphene will be rolled into a NT, and the atom at the tail of the wrapping vector will be bonded to the atom at the head of the vector. Using the unit vectors of the underlying lattice \mathbf{a}_1 and \mathbf{a}_2 (where $|\mathbf{a}_i| \sim 0.25$ nm), the wrapping vector can be written as a sum of integer multiples of these vectors: $n_1\mathbf{a}_1 + n_2\mathbf{a}_2$. Since the tube is derived from a two-dimensional plane, only two parameters are needed to uniquely describe the NT structure. While the wrapping index (n_1, n_2) is typically given, the tube diameter d (related to the wrapping vector length l by $d = l/\pi$) and the chiral angle (or helicity) ϕ is also sufficient. The chiral angle ϕ , defined as the angle between the wrapping vector and the unit vector \mathbf{a}_1 , is shown in Figure 2.1a. These indices can be used to uniquely describe and classify the electronic band structure in various NTs.

2.3 Band Structure of Graphene

In this section, we briefly present the results of tight-binding calculations (Ashcroft and Mermin 1976, McClure 1956, Wallace 1947) of the electronic structure of graphene. Since NTs are formed of rolled graphene, it is conventional to derive the NT band structure from the starting point of graphene. These calculations describe two bands (conduction and valence) that join at cones at the edge of the graphene Brillouin zone. These cones yield the linear energy dispersion of particles and antiparticles (electrons and holes) with zero effective mass. In Sections 2.4 and 2.5, we use the wave functions and band dispersion of graphene to derive the NT electronic structure.

Each carbon atom in the graphene lattice has four available valence electrons. Three of these electrons form the in-plane covalent C-C bonds, while the fourth forms a hybridized p_z orbital extending out of the plane. It is this out-of-plane orbital that forms the basis states of the tight binding calculation and ultimately results in conducting electrons in graphene. In tight binding calculations, we first define a unit cell and then compose a wave function that describes a linear combination of p_z orbitals and maintains the periodic symmetry of the lattice. Using the unit cell labeled in Figure 2.2a, we compose a Bloch-like wave function:

$$\psi_k(\mathbf{r}) = \sum_A \exp(i\mathbf{k} \cdot \mathbf{R}_A) X(\mathbf{r} - \mathbf{R}_A) + \lambda \sum_B \exp(i\mathbf{k} \cdot \mathbf{R}_B) X(\mathbf{r} - \mathbf{R}_B) \quad (2.1)$$

Where \mathbf{R}_A and \mathbf{R}_B are the positions of the A and B atoms, $X(\mathbf{r})$ is the p_z atomic orbital of an isolated carbon atom, and $\lambda \exp(i\mathbf{k} \cdot \boldsymbol{\rho})$ is the phase difference between the A and B atoms of the unit cell with displacement vector $\boldsymbol{\rho}$ between neighboring atoms.

We evaluate $E_k = \langle \psi_k | H | \psi_k \rangle$ to find the eigen-energies of the system. Ignoring overlap of the wave functions between neighboring A atoms (and similarly neighboring B atoms) and only including contributions from nearest neighbors (A atoms surrounded by B atoms) yields the allowed energies:

$$E_k = E_0 \pm \left| \sum_i t_i \exp(-i\mathbf{k} \cdot \boldsymbol{\rho}_i) \right| \quad (2.2)$$

Where E_0 is the energy of the isolated carbon p_z orbital energy and t_i is the transfer (or overlap) integral between carbon atoms. We can re-write this equation in scalar form in two dimensions k_x and k_y as:

$$E(k_x, k_y) = \pm t \sqrt{1 + 4 \cos\left(\frac{k_x a}{2}\right) \cos\left(\frac{k_y a \sqrt{3}}{2}\right) + 4 \cos^2\left(\frac{k_x a}{2}\right)} \quad (2.3)$$

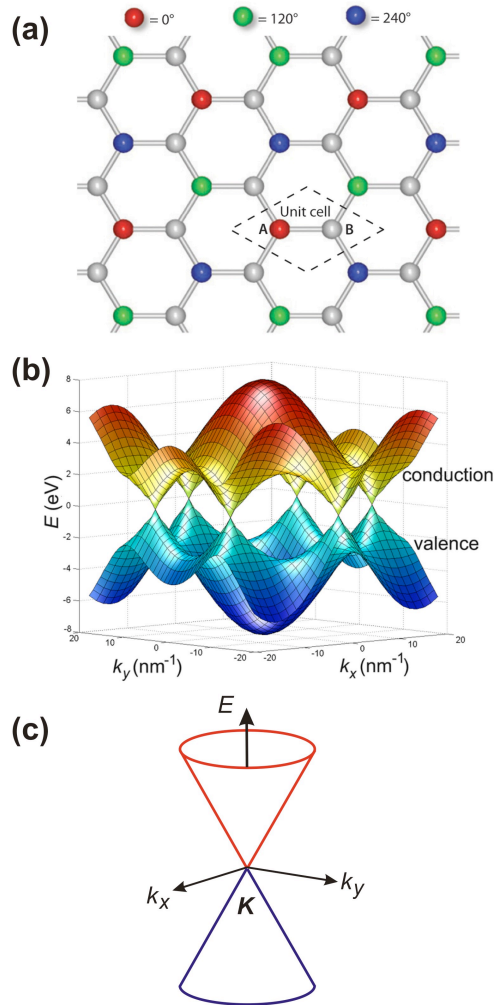


Figure 2.2. Graphene lattice and band structure. **(a)** The hexagonal C-C lattice showing the unit cell composed of A and B atoms. The wave function on the A atoms is color coded according to relative phase (labeled). A similar color code could be used for B atoms, but is not shown. **(b)** Calculated band structure of graphene using tight-binding calculations. **(c)** Conical energy dispersion (or Dirac cone) near the K-point in graphene. Images adapted from Ilani 2010 and Larrimore 2008.

where the overlap integral has the calculated value $t = -2.7$ eV (White and Mintmire 1998) and $a = |\mathbf{a}_i| = 0.25$ nm is the lattice vector in graphene.

The energy relation described in Equation (2.3) is plotted in Figure 2.2b. The positive solutions to Equation (2.3) give the conduction band, while the negative solutions give the valence band for graphene. These bands are symmetric above and below $E = 0$ which leads to charge carriers (electrons and holes) that have equivalent properties, differing only by the sign of charge.

Figure 2.2b also shows that near six particular k-space coordinates at the edges of the Brillouin zone, the conduction band and valence band meet and give $E = 0$. Near these six points in k-space, called the K-points, the energy dispersion is conical as shown in Figure 2.2c. Of the six touching K-points, only two are irreducible and are given the labels \mathbf{K} and \mathbf{K}' . Near these K-points the conical band has a slope $(\sqrt{3}/2)ta$ and Fermi velocity $v_F \sim 8 \times 10^5$ m/s. Since the effective mass of charge carriers is related to the curvature of the band dispersion, electrons and holes in graphene have zero effective mass. These linearly dispersive, massless carriers have been compared to relativistic charge carriers described by the Dirac equation, which has lead the energy dispersion relation to be called the Dirac cone. For most analyses, it is sufficient to use only these two non-equivalent K-points and the Dirac cones to understand the band structure of graphene and nanotubes.

2.4 Electronic Wave Functions in a Graphene Cylinder

Rolling graphene into a tube imposes boundary conditions on the electronic wave function of Equation (2.1). First, along the circumference of the tube, the crystal momentum becomes quantized since the wave function must match itself as it completes one full circulation. For a tube of diameter d , this gives the condition:

$$\Delta k_{\perp} \pi d = 2\pi \tag{2.4}$$

where k_{\perp} is the crystal momentum perpendicular to the tube axis. As shown in Figure 2.3 (inset), this quantization cuts a set of discrete planes out of the Dirac cone with a spacing defined by the above expression.

The intersection of planes at intervals of Δk_{\perp} with the allowed energies of the Dirac cone forms the one-dimensional subbands of NTs. In the direction parallel to the length of the tube, the wave function can take any value of k_{\parallel} , and leads to a continuum of energies. When a plane cuts through the tip of the Dirac cone, the resulting subband is linear down to $E = 0$. This forms a gapless (or metallic) subband. Conversely, if all planes miss the tip of the Dirac cones, the resulting tube has an energy gap and forms a semiconductor.

A full mathematical treatment of this zone-folding method of NT band structure yields a particularly interesting fact: 2/3 of all tubes are semiconducting while 1/3 are metallic. By making a simple observation about the electronic wave function near the K-point in graphene, a recent description by Ilani et al. (2010) gives a very intuitive way to see why this is so. Returning to the graphene lattice of Figure 2.2a, we show a color-coded map of the phase of the electronic wave function at all of the A atoms. From Equation (2.1) and the structure of the lattice, the A atoms have three possible phases 0 , $2\pi/3$, or $4\pi/3$ (0° , 120° , or 240°) which are color-coded red, green, or blue, respectively. When rolling the graphene into a cylinder, we match up A atoms to form the tube and consider how these phases will also match.

In the simplest case, a red atom is rolled up to match another red atom (Figure 2.3a). If this is the case, then the wave function near the K-point does not need to be altered, since it already describes an allowable wave function of the cylindrical system. The resulting wave function corresponds to a plane cutting through the tip of the Dirac cone at \mathbf{K} and thus a linearly dispersive metallic subband. Using the same analysis for B atoms leads to a similar result.

While the above case describes the simplest matching condition, there are two additional possibilities: rolling a green or blue atom onto a red atom (Figure 2.3b). In these cases, there is a phase mismatch of multiples of $2\pi/3$ that suggests that the wave function is no longer valid in the cylindrical geometry. To compensate for this mismatch, an additional term can be added to the

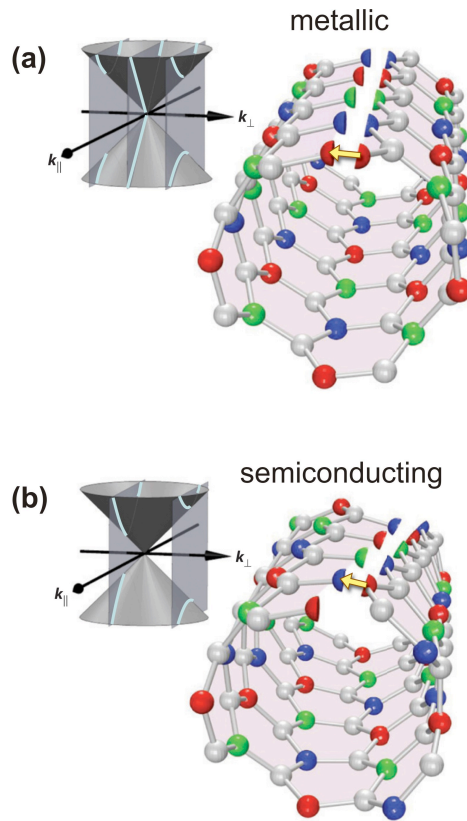


Figure 2.3. Rolling the graphene lattice into a tube. **(a)** The nanotube formed by matching a red atom of the graphene lattice to another red atom leads to a planar cut through the Dirac cone that intersects the K-point and results in metallic energy dispersion (inset). **(b)** Nanotube formed by matching a red atom to a blue atom creates a phase mismatch that must be compensated by appending the wave function. This leads to a planar cut away from the K-point and results in a gapped, or semiconducting, band (inset). Images adapted from Ilani 2010.

wave function. If this additional term in the wave function generates a phase that exactly compensates the phase mismatch over a single circulation of the tube, then the resulting wave function is valid in the cylindrical geometry. The simplest term that can compensate this phase mismatch is $\exp(ik_{\perp}^0 r_{\perp})$ where $k_{\perp}^0 \pi d = -2\pi/3$ describes the compensating phase matching condition and r_{\perp} is the circumferential direction. This term corresponds to an envelope to the wave function that acts to shift the wave function away from the \mathbf{K} -point by a distance $k_{\perp}^0 = 2/3d$ and generate a gapped (or semiconducting) subband (Figure 2.3b inset).

From the above discussion, it is now quite intuitive to understand why 1/3 of tubes are metallic and 2/3 are semiconducting. NTs that are constructed by folding a red atom onto another red atom are metallic, while folding a blue or green atom onto a red atom yields a semiconductor. Since each phase (each color) appears on only 1/3 of the lattice, metallic tubes occur in only 1/3 of the folding arrangements. In the remainder of our discussion, we focus only on semiconducting tubes, which make up the majority of NTs.

2.5 Band Structure of Semiconducting Nanotubes

As was discussed in the previous section, semiconducting behavior in NTs results from a planar cut through the Dirac cone that does *not* cut through the tip of the cone. Instead, due to the phase matching condition of the wave function when it is wrapped into a tube, the planar cut is displaced in k-space by a distance $k_{\perp}^0 = 2/3d$ (due to the phase mismatch of $2\pi/3$) forming a one-dimensional subband. As shown in Figure 2.4a, the plane that cuts through the cone at $k_{\perp}^0 = 2/3d$ forms the lowest energy subband, while the plane that cuts farther away from the k-point $k_{\perp}^1 = -4/3d$ forms the second subband. We can estimate the lowest lying energy state in a given subband (the band gap energy) by considering the slope of the Dirac cone $(\sqrt{3}/2)ta$ and the displacement in k-space ($k_{\perp}^0 = 2/3d$ for the closest planar cut). For the lowest energy subband, we see that

$$E_{GAP} = 2 \frac{\sqrt{3}ta}{2} \frac{2}{3d} = \frac{2ta}{d\sqrt{3}} = \frac{2ta_{C-C}}{d} \quad (2.5)$$

where t is the transfer integral, $a = |\mathbf{a}_i| = 0.25$ nm, $a_{C-C} = 0.14$ nm is the inter-atomic spacing, and d is the diameter. Subsequent planes that cut through the graphene dispersion at intervals of $\Delta k_{\perp} = 2/d$ form the increasing energy subbands and are generally labeled as E_{ii} where $i = 1, 2, 3$, etc. This result emphasizes a key property of NTs: the band gap energy (for all subbands) scales as $E_{GAP} \sim 1/d$.

Geometrically, planar cuts through the Dirac cone form hyperbolic one-dimensional subbands (Figure 2.4b). Following this geometric analysis, these subbands can be described very simply by adopting a hyperbolic model of the band structure:

$$\varepsilon_i(k) = \pm \sqrt{(m_i^* v_F)^2 + (\hbar k_{\parallel} v_F)^2} \quad (2.6)$$

where $v_F = 8 \times 10^5$ m / s is the Fermi velocity of graphene, \hbar is Planck's constant, $\hbar k_{\parallel}$ is the carrier momentum along the length of the nanotube and m_i^* is the effective mass of the i^{th} subband. As in the graphene dispersion, both positive and negative energy solutions are allowed (electrons and holes) and the subbands are symmetric above and below zero energy. The band gap energy $E_{GAP} = E_{11} = 2m_1^* v_F^2$ is the energy required to generate an electron-hole pair, while higher subband energies such as $E_{22} = 2E_{11}$ correspond to excitations of more massive particles ($m_2^* = 2m_1^*$). As is thoroughly discussed in many references (van Hove 1953, Dresselhaus 2001, Chapter 1), the one-dimensional subband energy gaps E_{ii} lead to van Hove singularities in the density of states. While very simple, this approximation of the band structure has been shown to be quite accurate for tubes of larger diameters when compared to more detailed band structure calculations (Zhou thesis 2007).

Equation (2.6) describes the energy of electrons and holes in a given subband as a function of the momentum along the NT length $\hbar k_{\parallel}$. From the geometric derivation of this band structure (Figure 2.4a), it is evident that each subband corresponds to a different transverse

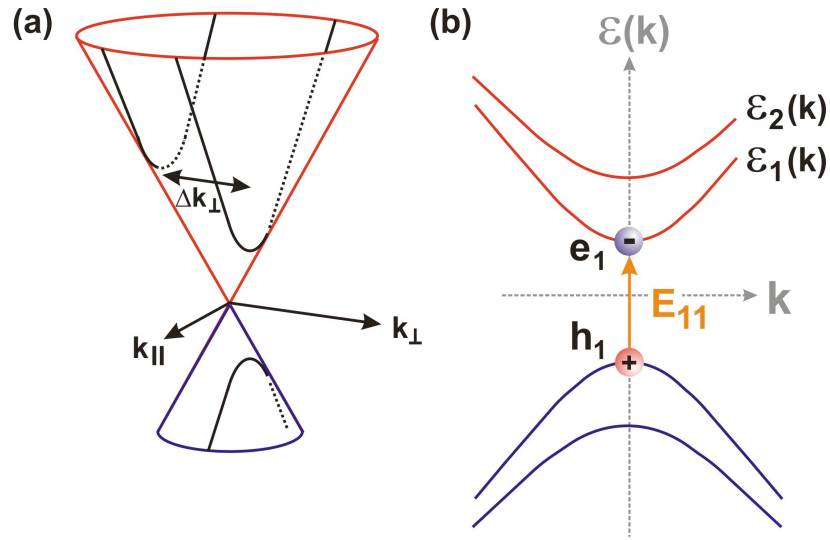


Figure 2.4. The semiconducting nanotube band structure. **(a)** The intersection of planar cuts through the Dirac cone results in hyperbolic one-dimensional subbands. The planes are separated by Δk_{\perp} in the k -space direction transverse to the nanotube axis. **(b)** The one-dimensional subbands are labeled $\epsilon_i(k)$ and the energy required to generate an electron-hole pair in the relevant band is E_{ii} .

momentum $\hbar k_{\perp}$ (implicitly contained in the effective mass of Equation (2.5)). Importantly, when interactions occur between electrons and holes in different subbands, energy and momentum must be conserved, both along the NT axis $\hbar \Delta k_{\parallel}$ and transverse to the NT axis $\hbar \Delta k_{\perp} = n \hbar (2/d)$ (where n is an integer corresponding to the relevant subband). As will be discussed in the next section, conservation of momentum and energy dictates the allowed interactions between subbands.

2.6 Carrier Interactions in NTs

In NTs, charge carriers that transit the one-dimensional conducting channel may collide with, create, or annihilate other fundamental quasi-particles. One such class of quasi-particles, acoustic and optical phonons, has been well studied and these phonons are known to interact strongly with high-energy electrons and holes in NTs. Although not discussed in detail here, these electron-phonon interactions often result in the absorption (annihilation) or emission (creation) of phonons.

In a similar process to phonon absorption and emission, electron-electron interactions in NTs may also lead to the absorption (annihilation) or emission (creation) of charged quasi-particles: electrons and holes. In low dimensional materials electron confinement and reduced electronic screening lead to drastically increased Coulomb interactions with energies proportional to e^2 / r where e is the electron charge and r is the distance between charges. To compare the energy scale of Coulomb interactions to a scale relevant in NTs, it is interesting to note that the hyperbolic bands of Equation (2.6) are analogous to the allowed energies of massive relativistic particles (positive solutions) and antiparticles (negative solutions) with relativistic energies mv_F^2 . In relativistic particle physics, the occurrence of charged particle interactions depends strongly on the ratio of the Coulomb interaction strength between electrons to their relativistic energies, and is quantified by the fine structure constant $\alpha = e^2 / 4\pi\epsilon_0 \hbar c \sim 1 / 137$, where ϵ_0 is the permittivity of vacuum. Interestingly, the small Fermi velocity and low dielectric

constant in NTs leads to an effective fine structure constant $\alpha = e^2 / 4\pi\epsilon \hbar v_F \sim 1$, suggesting that electron-hole creation and annihilation should be quite efficient.

In the remainder of this chapter, we focus on two processes that result from strongly interacting carriers: particle-antiparticle (electron-hole pair) creation and particle-antiparticle (e-h pair) annihilation. We present models of electron-hole pair creation (generally known as impact ionization in semiconductors) and electron-hole pair annihilation (commonly known as Auger recombination) in NTs. Drawing on the analogy of relativistic quantum mechanics and combining this with the physics of strongly interacting carriers in one dimension, we propose that NTs provide a highly interesting system in which to uncover new physical phenomena related to electron-electron interactions.

2.7 Carrier Interactions: Electron-Hole Pair Creation

In conventional semiconductors, conduction band electrons (and holes) can gain sufficient kinetic energy to collide with valence band carriers and generate an additional electron-hole (e-h) pair via impact ionization (Sze 1981). This process, shown in Figure 2.5a, converts excess kinetic energy into additional charge. In NTs, interactions between higher subband electrons and holes become important in the e-h pair creation processes, and one-dimensional momentum conservation must be considered. In this section, we describe the two lowest energy e-h pair creation processes that have been proposed in NTs. First, we describe a two-body creation process, first described by Kane and Mele (2003), by which a high-energy correlated e-h pair relaxes into two low energy e-h pairs. We then consider a three-body interaction, in which a highly energetic electron (or hole) relaxes to create a new electron and hole (Perebeinos et al. 2006).

In the NT band structure, the second subband $E_{22} = 2E_{11}$ corresponds to excitations of more massive particles ($m_2^* = 2m_1^*$). As shown in Figure 2.5b, an e-h pair initially at the second subband edge can relax into an electron-hole pair in the first subband with a finite kinetic energy.

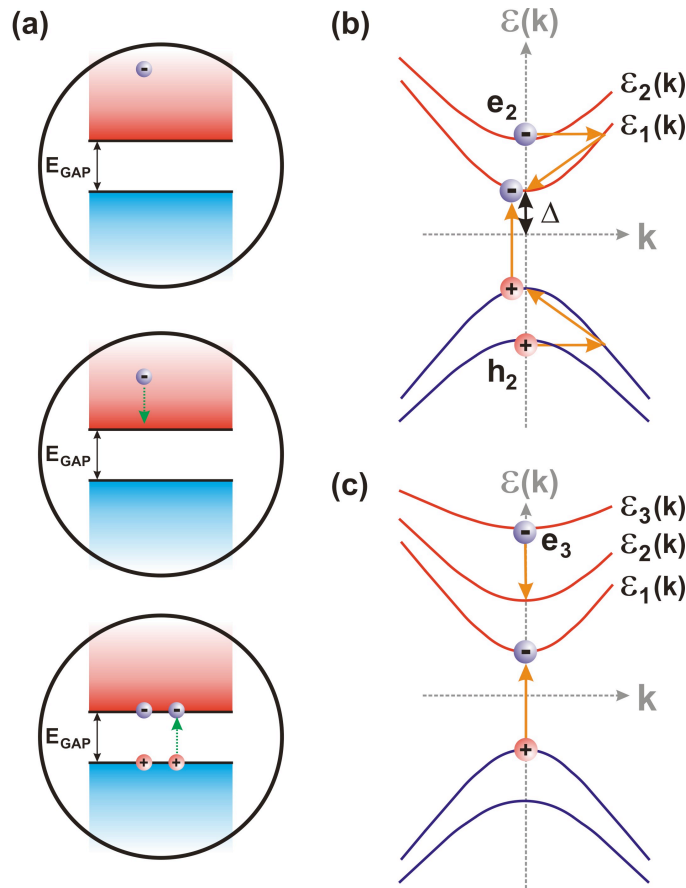


Figure 2.5. Electron-hole pair creation in carbon nanotubes **(a)** Schematic diagram of impact ionization in semiconductors. Excess kinetic energy is converted into additional charge. **(b)** Two-body e-h pair creation in nanotubes. One e-h pair in the second subband relaxes into two e-h pairs in the first subband. Due to strong Coulomb interactions, energy and momentum can be transferred between electron and hole. **(c)** Three-body e-h pair creation in nanotubes. A single electron in the third subband transfers momentum and kinetic energy to a first subband e-h pair.

Because $E_{22} = 2E_{11}$, this strongly interacting electron-hole pair has sufficient excess energy to relax into two e-h pairs via the process

$$e_2^2 + h_2^2 \rightarrow (e_1^1 + h_1^1) + (e_1^1 + h_1^1) \quad (2.7)$$

where the subscripts indicate the subband index and the superscript is the transverse momentum of the carrier in units of $2/(3d)$. While the transfer of the second subband e-h pair into two first subband pairs conserves energy, does it conserve momentum? Indeed, by transferring one unit of transverse momentum $\hbar\Delta k_{\perp} = \hbar(2/d)$ from the electron to the hole, this process simultaneously conserves energy and momentum. Kane and Mele studied this process analytically and showed that it may occur with high efficiency in the presence of strong Coulomb interactions between electrons and holes. Following Kane's analysis, strongly bound e-h pair correlations (excitons) in NTs have also been verified experimentally (Wang 2005).

We next turn to the lowest energy three-body process in which one energetic electron (or hole) creates two additional carriers. By considering strict conservation of energy and momentum in the NT band structure, Perebeinos et al. showed that e-h pair creation processes initialized from the first or second subband carriers of the NT band structure require excess kinetic energies that exceed many times the NT band gap energy and are inefficient at energy scales comparable to the band gap energy. However, simultaneous conservation of energy and momentum allows carriers in the third subband $\varepsilon_3(k)$ to undergo impact ionization via the process

$$e_3^4 \rightarrow e_2^2 + e_1^1 + h_1^1, \quad (2.8)$$

which occurs equivalently for holes. This process (shown in Figure 2.5c) converts an e_3 electron into an e_2 electron and an additional electron and hole in the first subband. As can be seen in Equation (2.8), the transverse momentum of the e_3 electron $4 * 2/(3d)$ is transferred to a second subband carrier (resulting in transverse momentum $2 * 2/(3d)$) and two first subband carriers.

While similar processes occur for higher subbands, this process is the lowest energy three-body creation process that conserves transverse momentum.

The efficiency of the two-body process of Equation (2.7) and the three-body process of Equation (2.8) both rely on strong Coulomb interactions. Equation (2.7) requires a strongly interacting electron and hole that can transfer energy and momentum within the correlated electron-hole pair state, while Equation (2.8) requires strong interactions between a high-energy electron and a valence band electron or hole. In Chapter 5, we present measurements that explore e-h pair creation processes and we compare our results to the models presented here.

2.8 Carrier Interactions: Electron-Hole Pair Annihilation

In the inverse process to impact ionization, electron-hole pairs can undergo non-radiative recombination by converting their potential energy into kinetic energy of a nearby free electron (or hole) via a process called Auger recombination (Sze 1981). As shown in Figure 2.6a, this process converts charge into kinetic energy. Similar to the e-h pair creation processes, Auger-like recombination can occur as a two- or three-body process. In this section, we first discuss the two-body annihilation process (considered theoretically by Valkunas et al. 2006, Ma et al. 2006, and Wang et al. 2006) and then follow with a discussion of the three-body process (Kinder et al. 2008).

Two-body annihilation in NTs occurs as the exact inverse of the two-body creation process of Equation (2.7):

$$(e_1^1 + h_1^1) + (e_1^1 + h_1^1) \rightarrow e_2^2 + h_2^2. \quad (2.9)$$

In this process, two low energy e-h pairs interact resulting in the recombination (or annihilation) of one e-h pair. The energy liberated is transferred to the remaining electron and hole (as shown in Figure 2.6b), and injects the carriers into the second subband. The wave vectors of the two outgoing particles can be chosen so that energy and momentum can be simultaneously satisfied

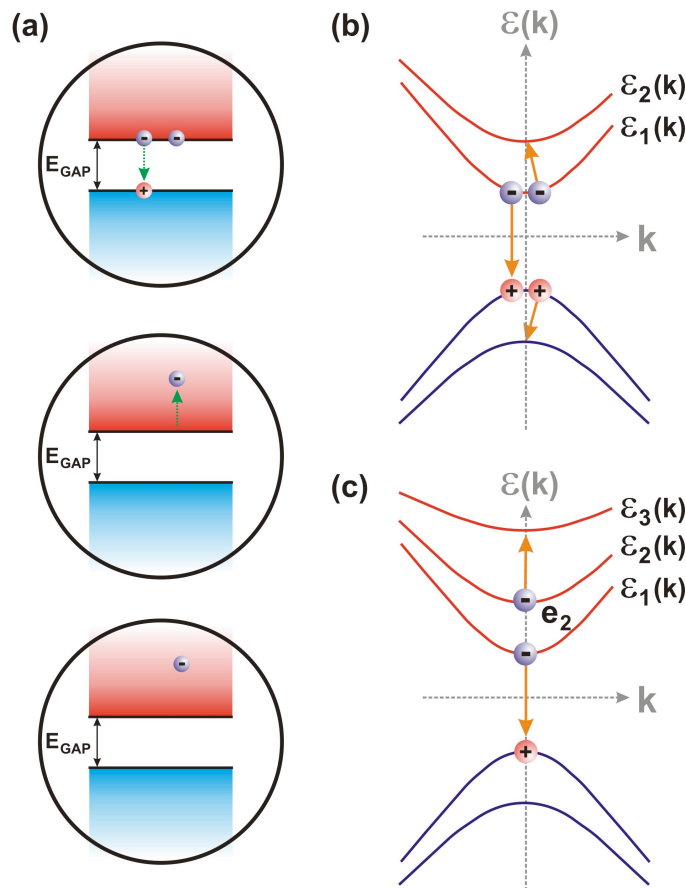


Figure 2.6. Electron-hole pair annihilation in carbon nanotubes **(a)** Schematic diagram of Auger recombination in semiconductors. Excess charge is converted into additional kinetic energy. **(b)** Two-body e-h pair annihilation in nanotubes. Two e-h pairs in the first subband interact leading to the annihilation of one e-h pair. The excess kinetic energy is transferred to the remaining e-h pair and converts it into a second subband e-h pair. **(c)** Three-body e-h pair annihilation in nanotubes. A first subband e-h pair self-annihilates and transfers momentum and energy to second subband electron. The remaining free electron is converted into a third subband carrier.

for any initial state. Since this process simultaneously conserves energy and momentum, it is completely non-radiative and is more efficient than processes that result in carriers with excess energy or momentum. While this process is the exact inverse of the creation process of Equation (2.7), it requires a high density of strongly interacting e-h pairs in the initial state. Quantum mechanically, the transition rate calculated by Fermi's Golden rule would be equivalent for Equation (2.7) and Equation (2.9), but the rate of the annihilation process depends on the initial population of e-h pairs.

We next discuss three-body electron-hole pair annihilation in which a free electron (or hole) interacts with a low energy electron and hole. This process results in only one outgoing particle and so puts constraints on the momentum and energy of the initial conditions. One possible process is the inverse of Equation (2.8)

$$e_2^2 + e_1^1 + h_1^1 \rightarrow e_3^4 \quad (2.10)$$

This process requires an initial e_2 carrier in order to undergo annihilation, but simultaneously satisfies momentum and energy conservation in the hyperbolic bands of Equation (2.6). A similar process involving carriers and e-h pairs in the lowest subband can also occur:

$$e_1^1 + e_1^1 + h_1^{-1} \rightarrow e_1^1 \quad (2.11)$$

According to analysis by Kinder et al. and Wang et al., this annihilation process satisfies energy and momentum conservation in parabolic bands, but does not satisfy these constraints in the fully hyperbolic band structure of NTs. In order for this process to occur in hyperbolic bands, neither the initial e-h pair nor the free carrier can initially exist at the bottom of the band and both must have significant excess kinetic energy many times larger than the band gap energy.

As was discussed in Section 2.6, the initial state of the e-h pair creation process is either a single electron (or hole) or a bound e-h pair that subsequently decays into additional e-h pairs. Unlike electron-hole pair creation processes, two- and three- body electron-hole pair annihilation

processes require a high density of initial carriers or e-h pairs to drive interactions. In Chapter 6, we describe ultrafast optoelectronic measurements that give evidence of these annihilation processes and compare and contrast our results to the models described here.

2.9 Conclusion

In this chapter, we presented a brief review of the theory of carbon nanotube band structure and presented a very intuitive geometric derivation of that band structure. By simply mapping the electronic wave function of graphene into a cylinder, we can immediately understand the hyperbolic one-dimensional bands in the carbon nanotube and draw an analogy to relativistic massive particles. The end of the chapter focused on the interactions of these massive relativistic particles and antiparticles by considering particle-antiparticle creation and annihilation. In Chapters 5 and 6, we will return to these ideas to understand the optoelectronic transport behavior in NT devices.

CHAPTER 3

INSTRUMENTATION: LOW TEMPERATURE SCANNING PHOTOCURRENT MICROSCOPE

3.1 Introduction

In condensed matter systems such as carbon nanotubes (NTs), experiments are designed to access elementary excitations at a broad range of energies. To study low energy electronic excitations in these systems, experiments are often conducted at liquid helium temperatures (and below) using precision electronics techniques. Such low temperature electronic measurements allow the thermal energy $k_B T$ (~ 0.1 meV at 1K) to go below the excitation energy of many elementary excitations, thus making them accessible to experiment. While electronic measurements focus primarily on exotic low energy excitations, optical measurements access excitations with energies comparable to visible or infrared photons ($E_{PHOTON} \sim 1-3$ eV). While purely electronic and purely optical experiments give complimentary insight into fundamental excitations, it is extremely important to understand the interplay of these excitations in novel nanoscale systems such as NTs.

This chapter discusses the experimental infrastructure that combines precision electronic and optical measurements at low temperatures to investigate nanoscale optoelectronic devices. In the following section, Section 3.2, we present a schematic description of the low temperature scanning photocurrent spectroscopy microscope. This microscope integrates low temperature electronics with spatially, spectrally, and temporally resolved optical illumination. After presenting a schematic description, the remainder of the chapter gives detailed descriptions of the various functional components of the microscope.

3.2 The Scanning Photocurrent Spectroscopy Microscope

The scanning photocurrent spectroscopy microscope (SPSM) combines electronics and optics to investigate optoelectronic behavior of nanoscale electronic devices (Figure 3.1). In the

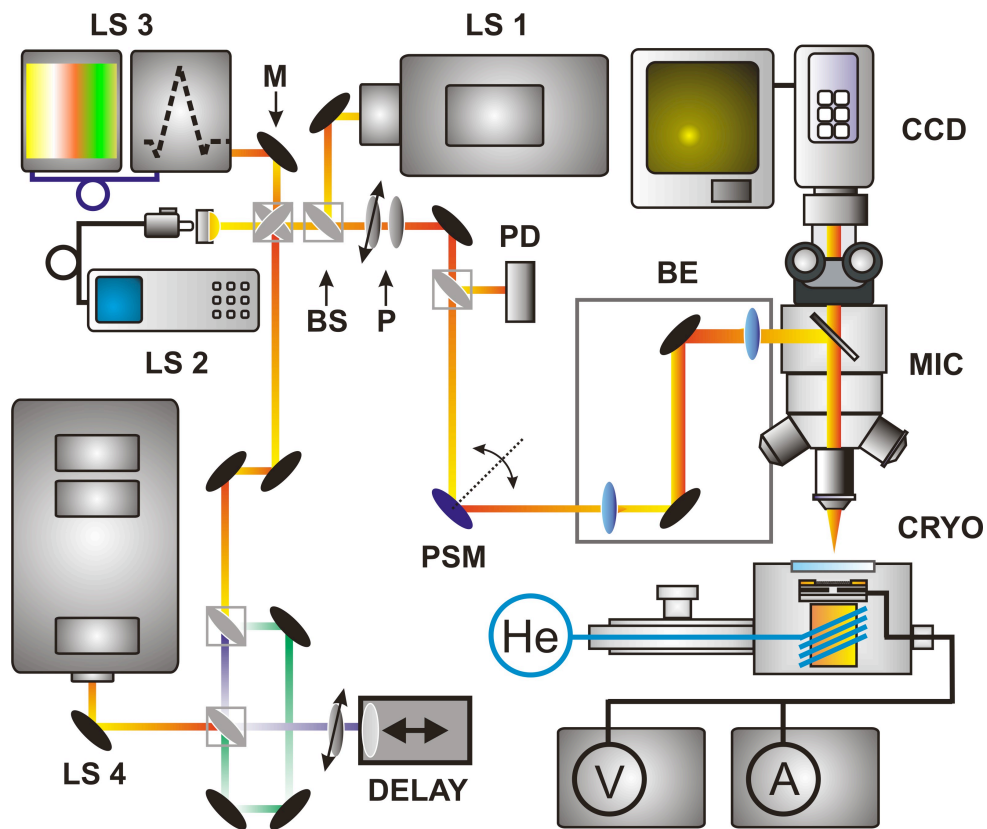


Figure 3.1. Schematic diagram of the scanning photocurrent spectroscopy microscope (SPSM). Electronic devices are mounted in the optical cryostat (CRYO) and optical illumination from various light sources (LS 1-4, described in text) is focused onto the device. The constituent components of the SPSM include: mirrors (M), beam splitters (BS), translation delay stage (DELAY), polarization optics (P), photo-diode detector (PD), piezo-scanning mirror (PSM), beam expander (BE), CCD camera (CCD), and microscope (MIC).

SPSM, nanoscale devices are wired into a helium flow cryostat (CRYO) equipped with a transparent window for optical access. This cryostat can be cooled to temperature $T \sim 4$ K and maintained at low pressures using a turbo pump system. Electronic feed-throughs provide electrical access to the device and allow the measurement of electronic properties while the device is illuminated at various temperatures.

To introduce light, a collimated optical beam is expanded (using beam expander BE) to fill the back aperture of the microscope objective (MIC), while a CCD camera is used to align the laser and image the device. A diffraction-limited beam spot can then be scanned (using a two axis piezo-controlled scanning mirror PSM) over the nanoscale device and the resulting current is recorded to form a spatial map of photocurrent. Photocurrent image resolution is limited by the wavelength of light used, and the beam spot diameter is determined from the full width at half maximum of the observed photocurrent spot. Reflected light from the sample is collected (as a photovoltage V_{REF} in a photo-diode detector PD) and the reflected intensity is monitored to form a simultaneous image of the device. The absolute location of the photo-induced signal is found by comparing the photocurrent map to the reflection image. Incident laser power is measured at the output of the microscope objective using a wavelength-calibrated photodetector.

The SPSM combines several light sources that can be aligned into the scanning microscope and focused onto the device. These include (1) a Melles-Griot Ar/Kr gas laser with 8 distinct wavelengths in the visible spectrum, (2) an Ando AQ4321 continuously tunable near infrared semiconductor laser ($\lambda = 1440-1620$ nm), (3) a Koheras SuperK compact supercontinuum light source with Princeton Instruments monochromator, and 4) a Coherent Ti:sapphire pulsed laser. As will be discussed in detail below, several different light sources are used to achieve high spatial resolution, tunability over a broad spectral range and at high spectral resolution, as well as ultrafast time resolution. By combining numerous light sources with low temperature electronics, this infrastructure allows versatile and in-depth experiments to be conducted on individual nanoscale optoelectronic devices.

3.3 Combining Low Temperature Electronics and Optics

In the following chapters of this thesis, we present electronic and optoelectronic measurements on individual nanotube (NT) devices (described in detail in Chapter 4). Before presenting experimental results, we first describe the low temperature probe station used for electronics measurements (presented in Chapter 4) and the Oxford HiRes optical cryostat used for optoelectronic measurements (Chapters 5 and 6).

Figure 3.2a shows a photograph of the Desert Cryogenics low temperature electronic probe station. Liquid helium is transferred from a 60 L Dewar into the transfer line of the probe station while the chamber is evacuated to a pressure $P \sim 10^{-6}$ mTorr. The temperature, which can be varied from $T = 4\text{-}350$ K, is controlled by a thermocouple heater located at the base of the cryostat and by regulating the helium flow through the transfer line. Helium flows continuously through the transfer line and cools a large metal plate at the base of the cryostat, upon which devices are placed in direct thermal contact. The probe station has four manually adjustable probe needles (tip diameter 10-50 microns), each of which is contacted electrically via external BNC connectors. In addition, the base plate of the cryostat can be used as a fifth large electrical contact. A window at the top of the cryostat allows visual inspection of the devices using a low magnification (4X) lens and CCD camera.

In order to combine controlled optical illumination with electronic measurements, we use a helium flow optical cryostat (Figure 3.2b). While virtually identical in function to the probe station, the optical cryostat provides several key advantages. First, the sample surface is separated from the outside of the cryostat by a very thin optical window. The ~ 1 mm thick window is composed of crystalline quartz glass and can withstand cryogenic vacuum. The total distance between the sample surface and the outside of the chamber is ~ 3 mm, a typical working distance for many microscope objectives. Second, the optical cryostat has 20 electrical contacts that can be soldered to a chip carrier and subsequently bonded to the device chip and secured to the sample plate of the cryostat (Figure 3.2b bottom). Using 20 electrical contacts allows several devices on a single chip to be solidly contacted via gold or aluminum wire bonds. Lastly, the

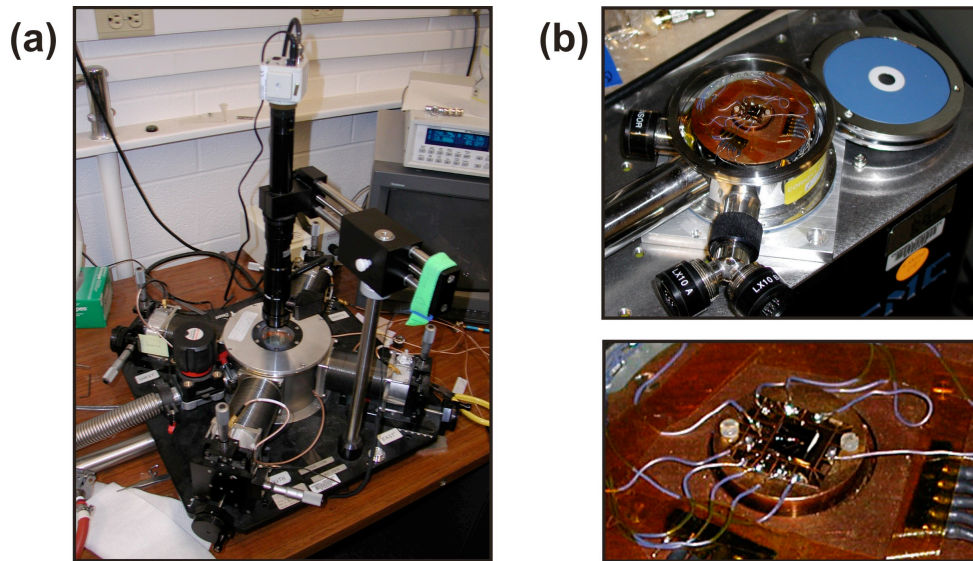


Figure 3.2. The low temperature electronic probe station and optical cryostat. **(a)** Desert Cryogenics 4K probe station used for electronics measurements at various temperatures. **(b) top.** Oxford optical cryostat used for low temperature optoelectronic measurements. **(b) bottom.** Zoomed image of the sample plate and sample holder in the optical cryostat. The device chip is mounted at the center and wire bonded to the sample holder, which is soldered to the electrical wiring of the cryostat.

small physical dimensions of the optical cryostat allow portability for experimental characterization and processing such as wire bonding, soldering, and leak detection.

The optical cryostat is mounted under an Olympus BX-51 microscope (Figure 3.3). Light enters from the side of the microscope via an access aperture and all manipulation of light (polarization, power attenuation, etc.) is done outside the microscope. Upon entering the microscope, the collimated light beam is reflected off a beam-splitter that reflects 95% (over a broad spectral range from UV to IR) of the light into the rear aperture of a microscope objective. The light is then focused to a diffraction-limited spot using one of several objectives. In the measurements described in this thesis, we use an Olympus UPLANFL 40X or 60X fluorescence microscopy objective with high numerical aperture (between 0.6 and 0.8) and long working distance of 2-4 mm. These objectives have uniform transmission over visible wavelengths and slowly decreasing transmission as the wavelength extends into the infrared (transmission $\sim 10\%$ at $\lambda = 1550$ nm). To compensate for optical aberrations caused by focusing light through a 1 mm thick glass window (the access window of the optical cryostat), the objectives include a corrector ring that adjusts internal optics to focus through the glass medium.

3.4 Spatially Resolved Laser Excitation

Figure 3.4 shows the key optomechanical and optical elements of the scanning photocurrent microscope. A collimated light beam from one of several light sources impinges on the scanning mirror after passing through a thin pellicle beam splitter. The scanning mirror (PSM) is composed of a two-axis piezo-mechanic silvered mirror (Physik Instrumente) that is actuated by a DC voltage amplifier. LabView control and data acquisition hardware provides these voltages as directed in software developed by the Park and McEuen groups at Cornell.

After reflecting from the scanning mirror, light is directed into a pair of achromatic doublet lenses before entering the microscope. This pair of lenses serves two vital roles for scanning photocurrent microscopy: beam expansion and beam translation. First, the focal length of these lenses is chosen to accurately expand the diameter of the beam to fill the 0.6 cm rear

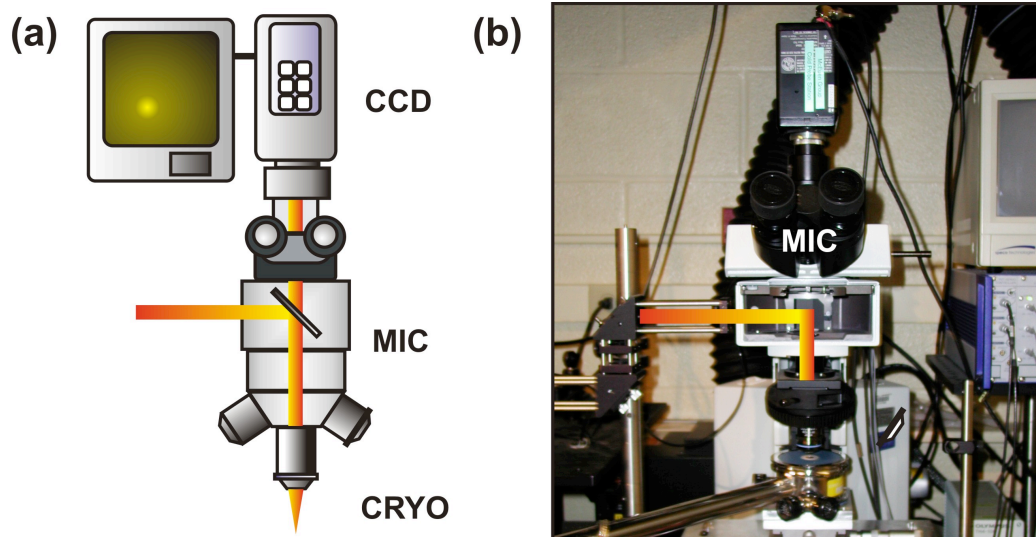


Figure 3.3. Schematic diagram (a) and photograph (b) showing the integration of low temperature electronics and optics. The optical cryostat is mounted under the microscope objective of an Olympus BX-51 microscope. Light enters from a side port and is reflected into the objective. A CCD camera is used to align the laser beam and image the device.

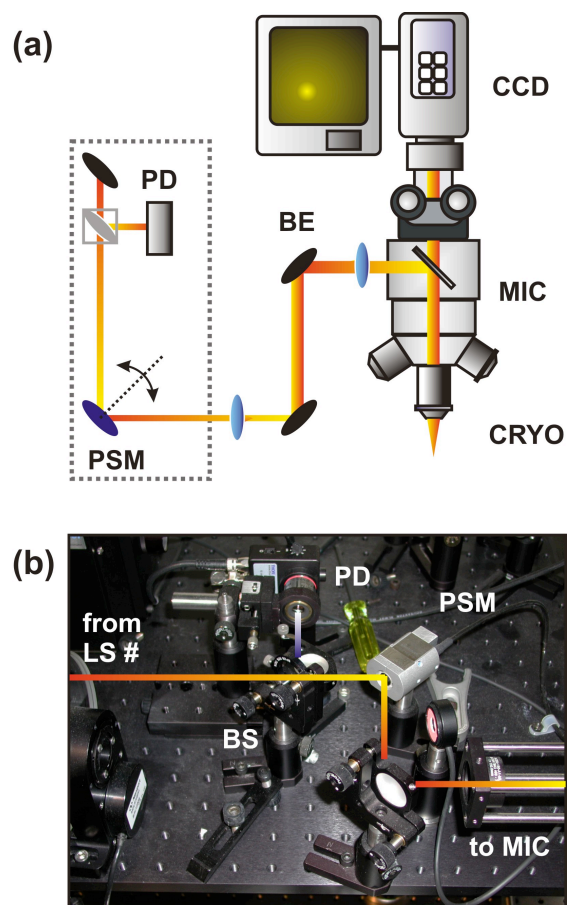


Figure 3.4. Schematic diagram (a) and photograph (b) of the essential components for scanning photocurrent microscopy. A collimated light beam is reflected from an electronically controlled scanning mirror and subsequently directed through a pair of achromatic doublet lenses. These lenses allow a diffraction-limited beam to be scanned across the sample surface at the output of the microscope objective.

aperture of the microscope objective. The ratio of the focal lengths is directly related to the magnification of the beam, and hence the expansion of the beam diameter. By filling the rear aperture, the optical power focused onto the device through the microscope objective is maximized.

The second and most important function of the achromatic doublet pair is to allow the laser beam to be accurately scanned on the device surface without beam distortion and aberrations. To see the importance of these lenses, we show a schematic in Figure 3.5. In the schematic, light impinges on the scanning mirror (PSM) and is reflected into the lens pair L1 and L2. This lens pair images the beam spot at the PSM directly to the rear aperture of the objective. When the collimated beam travels through the center of the lenses (orange dotted line), the collimated light is expanded, directed into the rear aperture of the objective, and focused to a diffraction-limited spot on the sample. When the collimated beam is deflected from the centerline, the light travels the path shown as a solid blue line in Figure 3.5. Of key importance, the expanded beam is still imaged to the rear aperture of the objective, but with an altered angle of incidence. On the sample, this change in the angle of incidence translates the focused spot, yet maintains a non-distorted Gaussian cross section. In this way, the actuating voltage applied to the PSM can controllably scan the spot across the sample while maintaining minimum aberrations and distortions.

In scanning photocurrent microscopy measurements (as described in the opening schematic of this chapter) the reflected light and the device current are simultaneously collected as the focused laser spot is scanned across the surface. The reflected photovoltage V_{REF} and the device current I are plotted as a function of two spatial coordinates to form a pair of correlated scanning photocurrent maps. These maps are then displayed and analyzed using LabView control software.

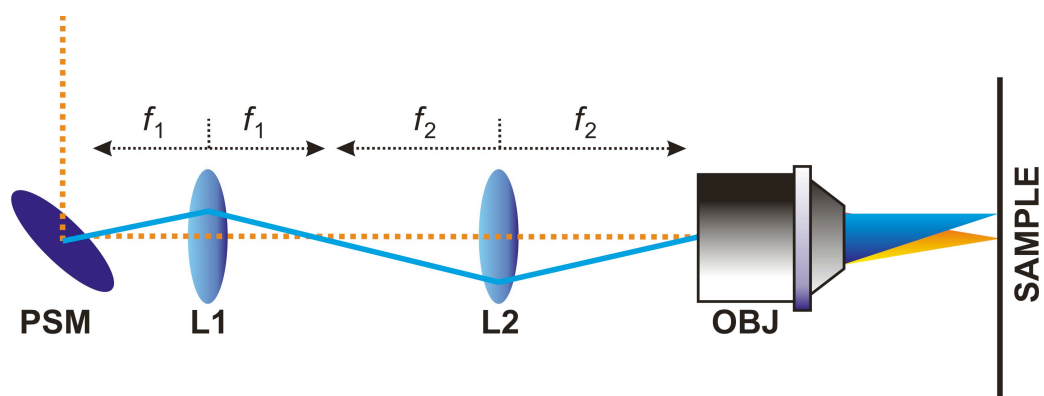


Figure 3.5. Diagram of the lens system required for scanning photocurrent microscopy. A light beam (orange dotted line) is reflected off the mirror (PSM) and travels through the center of the two achromatic doublet lenses (L1 and L2). These lenses magnify the beam to match the rear aperture of the objective (OBJ). By tilting the mirror, the beam is deflected (blue solid line), which translates the focused laser spot across the sample surface.

3.5 Spectrally Resolved Supercontinuum Excitation

One of the most powerful tools in the scanning photocurrent spectroscopy microscope is the supercontinuum light source. In the supercontinuum generation process (Lin et al. 1976, Birks et al. 2000), a temporally narrow laser pulse passes through a strongly nonlinear optical medium. Due to strong chromatic dispersion for short light pulses in the medium, the light at the output has a very broad spectral bandwidth and corresponding low temporal coherence. However, the light at the output maintains strong spatial coherence and large optical power, much like a laser. In the light source used for this thesis (Koheras SuperK), a pulsed laser pump (repetition rate = 25 KHz, pulse width = 2 ns) is launched into a micro-structured optical fiber (the non-linear medium) of 1 meter length. At the output of the fiber, the collimated white light beam has an average power $P > 100$ mW that ranges from $\lambda \sim 450$ -2000 nm, yielding a resolving power of about 25 μ W/nm in the visible range.

In order to spectrally resolve the supercontinuum light, we couple the optical fiber directly to a Princeton Instruments monochromator (Figure 3.6). Incoming light at the entrance slit of the monochromator is directly imaged to the exit slit after passing through a diffraction grating (DG). In the coupling scheme shown in Figure 3.6, the numerical aperture of the optical fiber matches the effective numerical aperture of the monochromator lens system. Due to this match, the light cone exiting the fiber at the entrance slit fully fills the parabolic mirror M1. The parabolic mirror *M1* collimates the light and reflects it directly to the diffraction grating, after which the white light is spatially separated into its constituent spectral components. After passing through the grating, light is then re-focused by parabolic mirror M2 onto the exit slit. A motorized controller adjusts the angle of the diffraction grating to align the spectrally separated light components towards the exit slit, while a micrometer-controlled slit is used to narrow the output spectral distribution. After the exit slit of the monochromator, a 10X Olympus objective (not shown) collimates the spectrally resolved light. As shown in Figure 3.1, the collimated light from the supercontinuum/monochromator system is directed into the optical path leading to the microscope. At the sample surface, the optical power density at maximum spectral resolution is

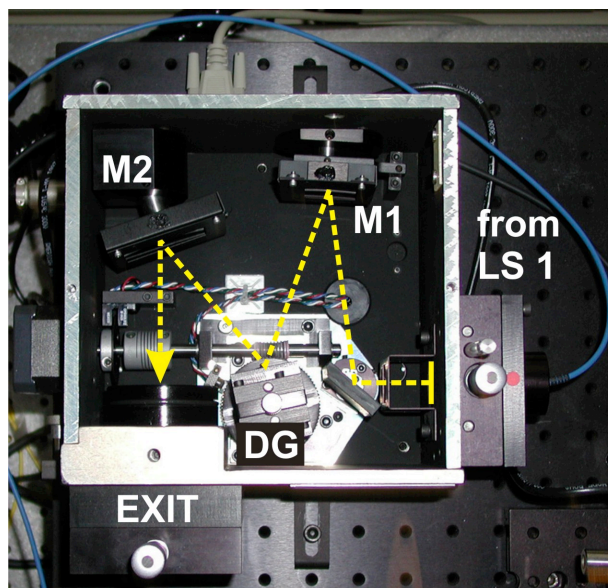


Figure 3.6. Photograph of the supercontinuum optical fiber (blue) coupled to a monochromator for spectrally resolved excitation. The dotted arrow traces out the trajectory of light through the monochromator. White light entering (at right) is reflected off the parabolic mirror (M1) and separated into its spectral components at the diffraction grating (DG). The light is then focused by another mirror (M2) to the exit slit of the monochromator. At the exit, an adjustable slit removes extraneous spectral components of the dispersed light. The light is then collimated by a 10x objective just outside the monochromator (not shown).

$\sim 3 \text{ W/cm}^2\text{-nm}$ over most of the visible and IR spectral range. For the measurements presented in this thesis, we measure the optoelectronic device current as the wavelength (photon energy) is continuously tuned over the range of the supercontinuum source.

3.6 Temporally Resolved Ultrafast Laser Excitation

In the final section of this chapter, we describe the ultrafast laser source and two-pulse time delay scheme used to temporally resolve optoelectronic device response at low temperature. We use a Coherent titanium:sapphire laser that is optically pumped by a Verdi V5 5 Watt green laser. The resultant light pulses are emitted from the cavity at a repetition rate of 75 MHz and a temporal width of $\sim 180 \text{ fs}$. As shown in Figure 3.7, a combination of simple optical components and a motorized translation stage allows the laser to function in single-pulse mode or, alternatively, a double-pulse mode in which two subsequent pulses are separated by a short time delay.

In the single-pulse mode, the laser beam exits the cavity (LS4), bypasses the optics shown in Figure 3.7, and is directed into the microscope to be focused onto the device. The power is attenuated using a thin film neutral density filter and is measured at the output of the microscope objective. Importantly, a Faraday isolator is placed at the exit of the laser cavity to prevent the back-reflected laser beam from entering the cavity and interfering with the mode-locked pulses.

In double-pulse mode, the single pulse laser passes through a beam splitter (BS) and is split into a reference beam and a delay beam. The reference beam is reflected from two adjustable mirrors before being recombined with the delay beam at a second beam splitter. The delay beam is directed into a retro-reflective mirror that is supported on a Thorlabs motorized delay stage. Using the $\sim 3 \text{ cm}$ of available stage translation, the optical path length of the delay beam can be varied up to $\sim 6 \text{ cm}$. This corresponds to a maximum time delay of 200 picoseconds relative to the reference beam. After the optical path length is adjusted in the delay beam, the two beams are recombined forming a two-pulse train in which two 180 fs pulses are separated by

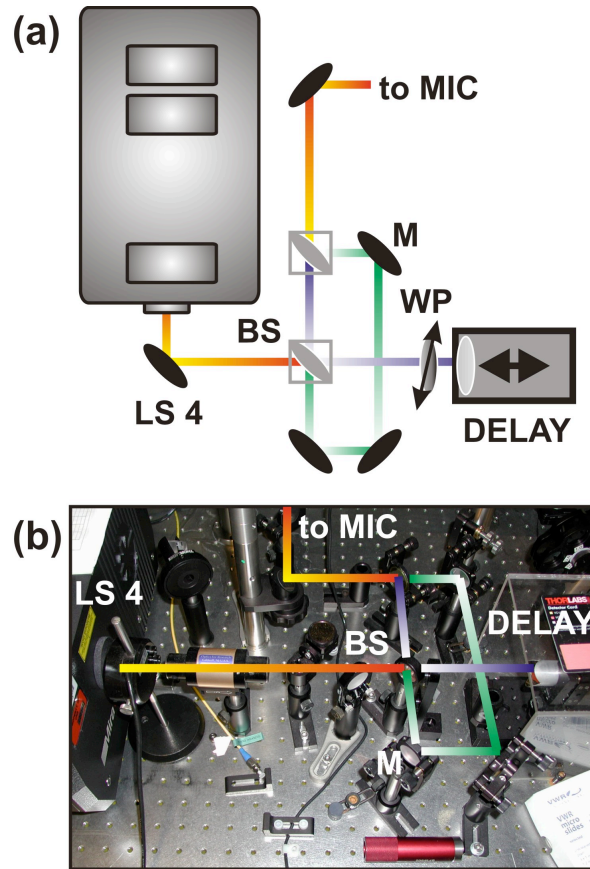


Figure 3.7. Schematic diagram (a) and photograph (b) of the optical and optomechanical components for temporally resolved laser excitation. An ultrafast laser beam is split (via beam splitter BS) into a reference beam (green beam) and a delay beam (blue beam). The optical path of the delay beam is electronically controlled by a translation stage (DELAY), after which the beam is recombined with the reference beam. The pulse train, composed of two pulses separated by a small time delay, is then directed into the microscope and focused onto the optoelectronic device.

a time delay ranging from 0-100 ps. In experiments, the pulse train generated by the delay is sent into the microscope and focused onto the device. The photocurrent is then measured as a function of the delay time.

3.7 Conclusion

The scanning photocurrent spectroscopy microscope discussed in this chapter is the primary experimental tool developed and used for the work presented in this thesis. By combining spatially, spectrally, and temporally resolved laser excitation, we have a full suite of experimental parameters to investigate the optoelectronic behavior of nanoscale devices at low temperatures. The remaining chapters highlight a set of in-depth experiments conducted on a novel optoelectronic device: the carbon nanotube PN junction.

CHAPTER 4

ELECTRONIC TRANSPORT IN THE NANOTUBE PN JUNCTION

4.1 Introduction

Since their discovery, carbon nanotubes (NTs) have intrigued many in the scientific and technology communities, particularly for their promise for electronics at the nanoscale. The first NT field effect transistors (FETs) were investigated just over a decade ago (Tans et al. 1998), and subsequent research has focused intensely on device applications (Bachtold et al. 2001, Liang et al. 2001, Javey et al. 2002, Rosenblatt et al. 2002). After demonstrations of FET devices, research focused on another highly important electronic device: the semiconductor PN junction. Early work introduced vaporized potassium to achieve n-type (negatively charged) carrier doping on a segment of NT adjacent to a p-type (positively charged) segment and demonstrated electrical rectification (Zhou et al. 2000). Later, by exploiting the interplay of mechanical deformation and electronic properties, Minot et al. used atomic force microscopy (AFM) measurements to demonstrate mechanically induced PN junctions and studied the transmission of electrons through these barriers (Minot et al. 2003). More recently, Lee et al. utilized local electrostatic gating, similar to that used in FETs, to demonstrate carefully controlled PN junctions and showed that these devices operate with ideal diode behavior (Lee et al. 2004).

In this chapter, we describe electronic transport measurements on individual NT PN junctions formed by electrostatic gating. We measure the electronic characteristics at various temperatures and in various regimes of applied bias and gate voltage. In forward bias, we observe strong temperature dependence that is well described using a one-dimensional model for electron transit over a potential barrier. From our analysis, we can directly extract the band gap energy and the electronic transmission coefficient for electrons and holes through the PN junction. Lastly, we measure the high reverse bias breakdown of these devices and summarize

the measured and analytically extracted device parameters. The main results of this chapter were published in Bosnick, Gabor et al. (2006).

4.2 Device Fabrication

As described in Chapter 1, the samples measured in this thesis consist of individual semiconducting NTs integrated into a buried split-gate geometry that allows local electrostatic doping along the channel length (Figure 4.1). Fabricating buried device gates and synthesizing NTs on the top surface of the device allows us to introduce various experimental probes (such as AFM and focused laser light) to the NT channel. In the following, we describe the basic fabrication process (adapted from Lee et al. 2004), which consists of 3 stages: 1) Fabricating buried split-gate substrates, 2) Growing NTs, and 3) Fabricating electrical contacts to the NTs.

To fabricate the underlying split-gate substrate, we first deposit 50 nm-thick molybdenum metal gate electrodes on a Si/SiO₂ wafer using electron beam evaporation. Subsequently, plasma enhanced chemical vapor deposition (PECVD) is used to deposit a 100nm-thick SiO₂ layer (Figure 4.1a). To prepare the substrate for NT growth, the substrate is then diced into ~2 cm² chips and plasma-cleaned in oxygen plasma for 60 seconds.

Nanotubes are grown on the split-gate substrate using the flying catalyst chemical vapor deposition (CVD) growth process (Kong et al. 1998), shown schematically in Figure 4.1b. Using a liquid precipitation method, Fe/Alumina nanoparticles in water solution are deposited at lithographically defined sites on the substrate. The nanoparticles act as catalysts, from which NTs are grown when subjected to an environment of hydrogen and ethylene (or methane) gas at 915 degrees Celsius for 10 minutes. The resultant NTs have lengths up to 10 microns and a diameter distribution centered at 1.5 nm with a range extending from 1-4 nm.

In the final fabrication step, we fabricate gold (5 nm Cr adhesion layer + 50 nm gold) electrodes on top of the NT devices (Figure 4.1c) (Rosenblatt et al. 2002). Before evaporating the contact metals via e-beam evaporation, a buffered oxide etch is used to expose the split gate electrodes. The electrodes are patterned on top of the catalyst sites and over the exposed split

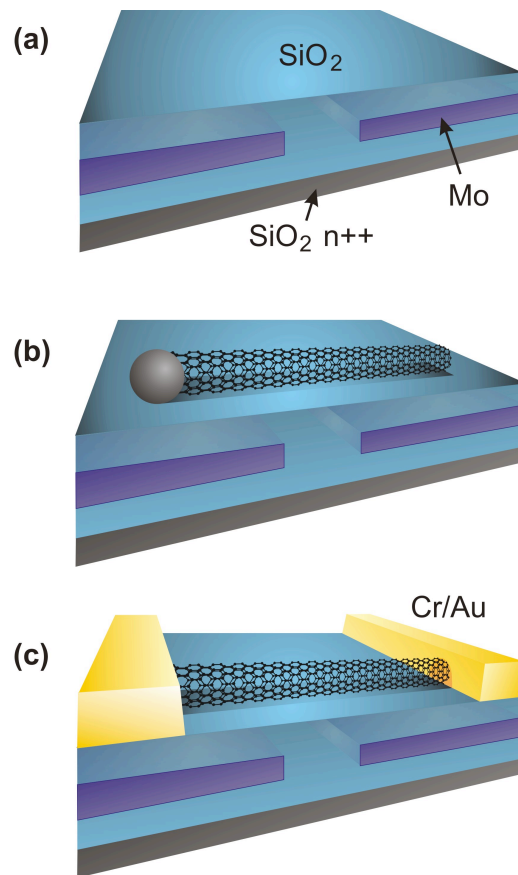


Figure 4.1. Schematic diagram of the fabrication process for multiple gate nanotube PN junction devices. In the first stage **(a)**, molybdenum gates are deposited on the native oxide of a silicon wafer, and then covered with silicon dioxide via plasma enhanced chemical vapor deposition. **(b)** Individual nanotubes are then grown from islands of iron catalyst particles (schematic includes only single catalyst particle). Finally **(c)**, gold electrodes are deposited over the nanotube and annealed to yield low electrical contact resistance.

gate contacts resulting in a 3 micron separation between contact electrodes. We then probe electrical conductivity of the device junctions to identify those containing one or more NTs and measure the NT diameters using AFM. Transistor characteristics are measured by sweeping the voltage on the Mo split gates (V_1 and V_2) and the Si back gate (V_G) together. All of the devices used in this work show a significant "off" region between n-type (positive gate voltage) and p-type (negative gate voltage) conduction behavior indicating semiconducting behavior.

4.3 Device Characteristics and Gate Dependence

We first measure the electrical current I of the NT PN junction as a function of source drain voltage (V_{SD}) and back gate voltage (V_G). Figure 4.2 shows I - V_{SD} characteristics for a typical device at $T = 260$ K and $T = 20$ K with the split gates oppositely biased. The device is strongly rectifying, turning on at less than 1 V in the forward bias direction, but with no significant current in reverse bias until about -9 V. The effect of varying the back gate voltage is shown in Figure 4.3 for a similar device at $T = 120$ K. The device I - V_{SD} behavior is significantly different when V_G is grounded (i.e. $V_G = 0$ V) and when it is equal to V_1 or V_2 . In the former case, the region of the NT between the split gates of the device is intrinsic (forming a p - i - n junction), while in the latter cases this region is p - or n - type (p - p - n or p - n - n junction). In the p - p - n or p - n - n configurations, the device "leaks" in both the forward and reverse bias directions as shown in Figure 4.3b; that is, it begins conducting at much lower bias voltages than in the p - i - n configuration. The good diode behavior, with strong rectification as shown in Figure 4.2, requires a significant intrinsic region between the p - and n - type regions. For the results presented in this thesis, we use the transport characteristics similar to those in Figure 4.3 to characterize and optimize the PN junction and focus primarily on devices measured in the p - i - n configuration.

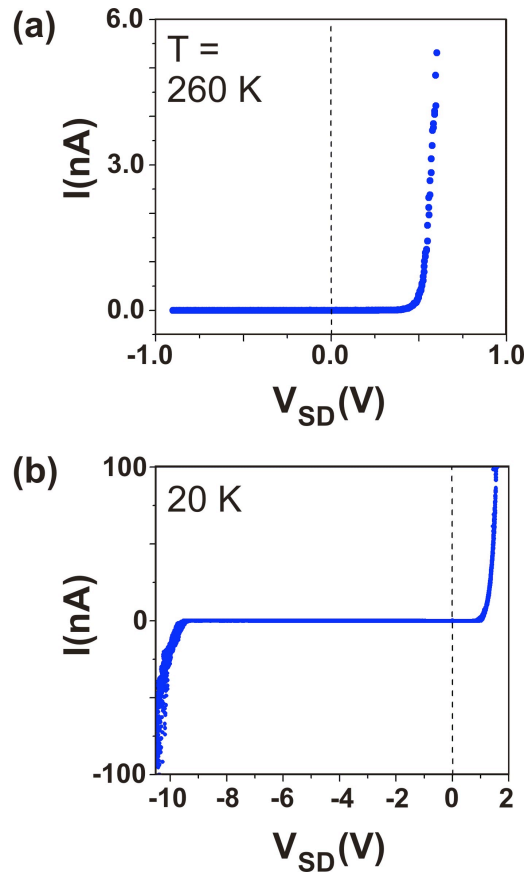


Figure 4.2. I - V_{SD} characteristics of the NT PN junction at (a) $T = 260$ K and (b) $T = 20$ K. In forward bias, the device turns on below 1 V, while in reverse bias the device shows no significant current until the voltage exceeds ~ 9 V. This asymmetry is a typical characteristic of current rectification in conventional diode devices.

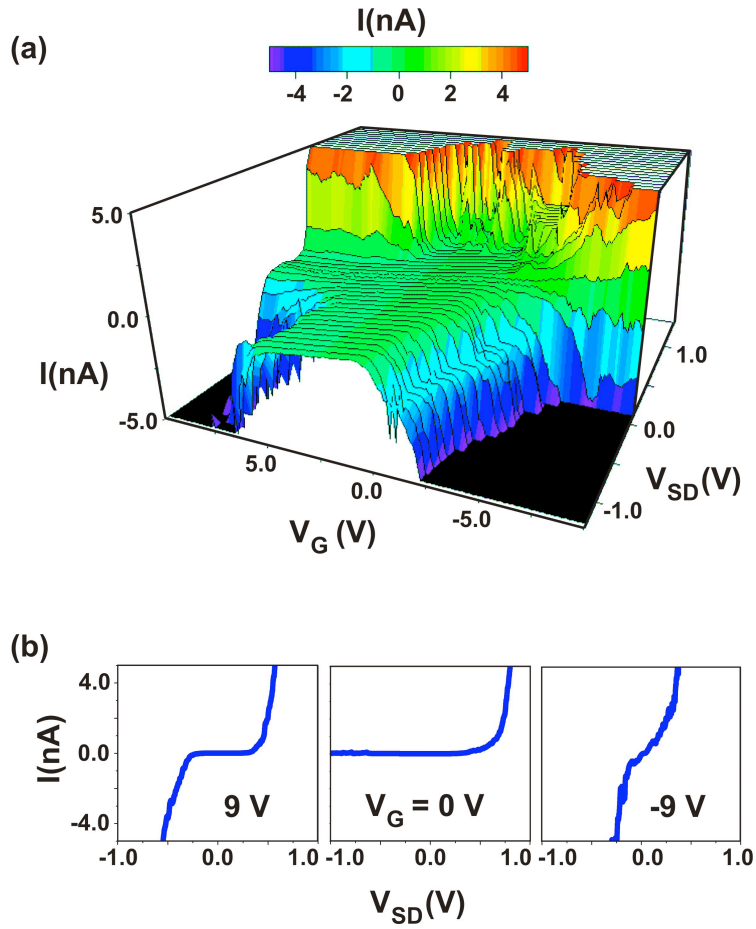


Figure 4.3. (a) I - V_{SD} characteristics as a function of back gate voltage V_G for the NT PN junction at $T = 120$ K. V_1 and V_2 are set at opposite polarities ($V_1 = -V_2 = 10$ V) and V_G is varied from -10 to 10 V. (b) I - V_{SD} characteristics at different back gate voltages. The PN junction shows the best diode behavior (i.e. asymmetric characteristic) when $V_G \sim 0$ V, and the device is configured into a p - i - n junction.

4.4 Forward Bias: Temperature Dependence Measurements

Once the PN junction has been optimized, we measure the device transport characteristics in forward bias. This section describes the main experimental results of this chapter: the temperature dependence of the I - V_{SD} characteristics. In Figure 4.4a, we show the forward bias I - V_{SD} characteristics for a nanotube with approximate diameter of 1.6 nm. By comparing characteristics at two temperatures in a log scale, we see that the low forward bias current increases exponentially with a slope that changes with temperature T . At higher current values, we find that the data fall below this exponential increase. From measurements of many devices, we find that the crossover between exponential increase and sub-exponential behavior depends weakly on temperature and back gate voltage, but typically occurs at ~ 1 nA.

We next focus on the initial exponential increase of the I - V_{SD} characteristics. As seen in Figure 4.4c, we measure I - V_{SD} characteristics at a variety of temperatures, and observe that as temperature decreases, the current-voltage slope increases. As shown in the inset of Figure 4.4c, the inverse of the slope varies linearly with temperature T (Figure 4.4c inset): $\alpha = dV / d \ln(I) \sim 1.2 K_B T$.

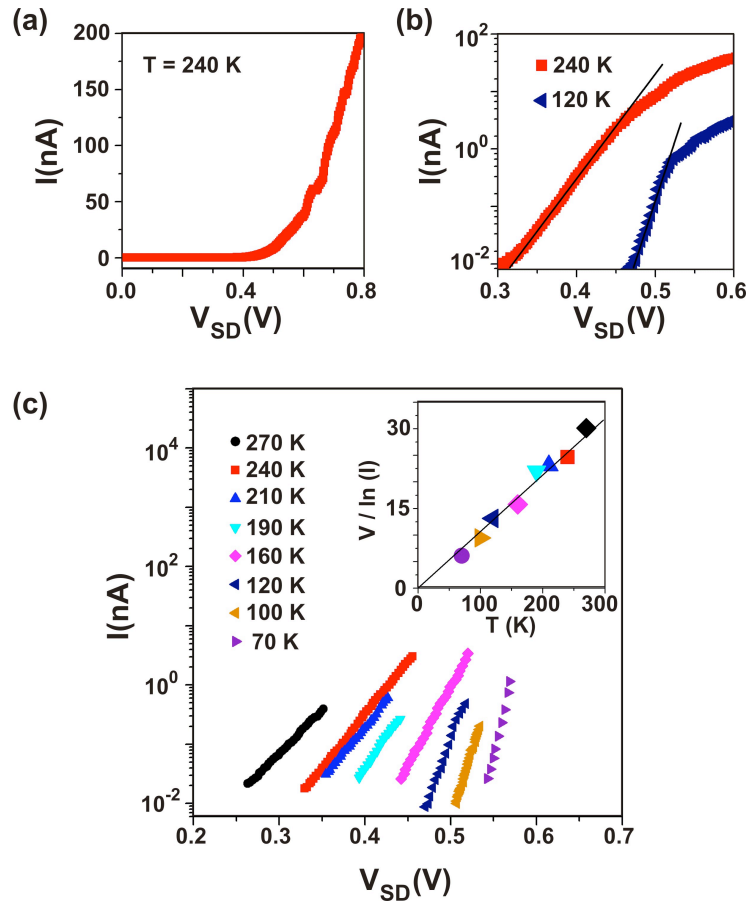


Figure 4.4. Temperature dependence of the forward bias I - V_{SD} characteristics. **(a)** I - V_{SD} characteristics for a device of diameter $d = 1.6$ nm at low temperatures ($T = 240$ K). **(b)** I - V_{SD} characteristics for the same device plotted in a semi-logarithmic scale at $T = 240$ K and at $T = 120$ K. Lines are drawn over the exponential portion of the I - V_{SD} characteristics. **(c)** Exponential portion of the I - V_{SD} characteristics for the same device over a wide temperature range. **Inset.** The inverse slope of the exponential portions as a function of temperature.

4.5 Model: Thermal Activation Across a One-Dimensional Barrier

In the NT PN junction, exponential behavior with V_{SD} has previously been observed at room temperature (Lee et al. 2004). Lee et al. used the ideal diode equation, $I = I_0(\exp(eV/nk_B T) - 1)$, to fit the characteristics and extract the diode ideality factor n . In the ideal diode equation, n describes the relationship between applied bias and the thermal energy of the system. A device yielding $n = 1$ is said to be an ideal diode. In our work, we use measurements over a wide range of temperatures in conjunction with a diode model based on the one-dimensional Landauer formula to extract all the important parameters of the device.

Ignoring any recombination between electron and hole bands, the current given by the Landauer-Buttiker formalism (see Chapter 1) is

$$I \approx (4e/h) \int_{-\infty}^{\infty} \mathfrak{S}(E, V) [f_D(E) - f_S(E - eV)] dE \quad (4.1)$$

To simplify the analysis, we model the diode to have a transmission coefficient \mathfrak{S}_0 for energies above the band gap (for electrons) or below the band gap (for holes). Ignoring the contribution to device current from tunneling and assuming E_{GAP} and $eV \gg k_B T$, a straightforward calculation yields

$$I \approx (8ek_B T/h) \mathfrak{S}_0 \exp[(eV/n - E_{GAP})/k_B T] \quad (4.2)$$

where $n > 1$ is a phenomenological factor that relates the applied voltage to the lowering of the effective barrier for electrons and holes (Figure 4.5).

Interestingly, Equation (4.2) predicts that a plot of $I / (8ek_B T/h)$ vs. V_{SD} taken at different temperatures will all meet at a single voltage and current given by $V = nE_{GAP}/e$ and $I/(8ek_B T/h) = \mathfrak{S}_0$. In Figure 4.6, we re-plot the data of Figure 4.4c and see that the data indeed exhibits behavior consistent with Equation (4.2): First, comparison of the data in the inset of Figure 4.6 with Equation (4.2) yields $n = 1.2$ for this device. Second, all the characteristics indeed meet at a

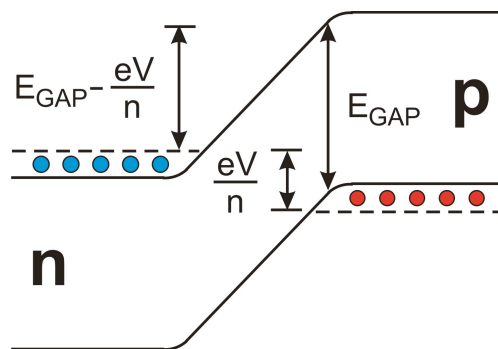


Figure 4.5. Schematic diagram of the PN junction used to derive Equation (4.2). The electrons must subtend the potential barrier at the PN junction to reach the opposite device contact. The barrier height can be estimated as the band gap energy E_{GAP} minus the applied voltage and Equation (4.2) can be derived assuming a Boltzmann distribution of carriers at energies above the Fermi energy.

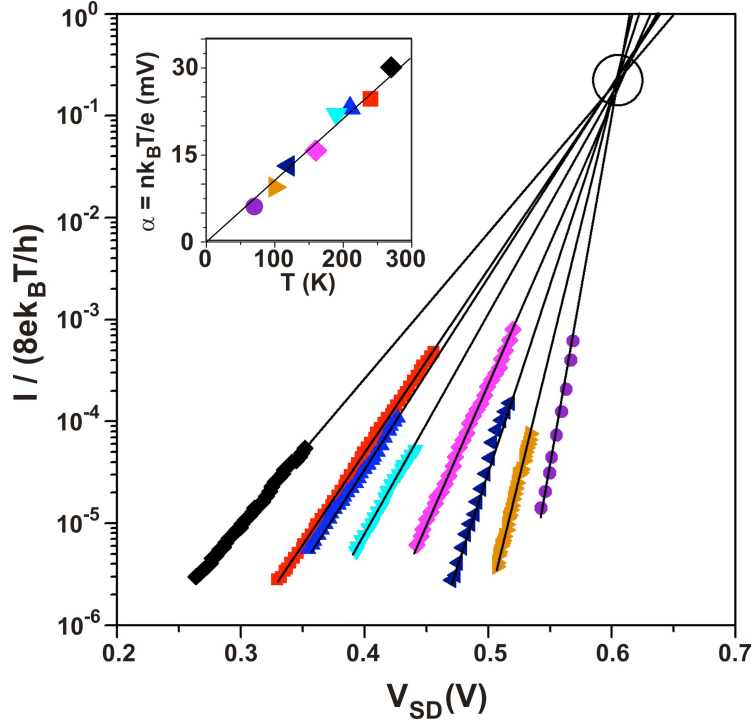


Figure 4.6. Temperature dependence of the forward bias I - V_{SD} characteristics of the NT PN junction. To compare to Equation (4.2), the current I is divided by $8ek_B T/h$. All characteristics meet at a voltage of $V_{SD} = 0.61$ V and a current of $I = 0.2$ ($8ek_B T/h$). **Inset**, the inverse slope as a function of temperature determines the constant n . From n and the current-voltage intersection we can determine the band gap $E_{GAP} = 0.61$ eV / $n = 0.51$ eV and the transmission coefficient $\mathfrak{F}_0 = 0.2$.

voltage of $V_{SD} = 0.61$ V and a current of $I = 0.2$ ($8eK_B T/h$). From this intersection, we are able to infer the band gap $E_{GAP} = 0.61$ eV / $n = 0.51$ eV and the transmission coefficient for electrons through the junction $\mathfrak{S}_0 = 0.2$. Table 4.1 shows the inferred parameters E_{GAP} , \mathfrak{S}_0 and n for four NTs of different diameters.

The band gap obtained from the transport measurements can be compared with the theoretical prediction E_{GAP} (theory) ~ 0.7 eV/ d [nm]. For the $d = 1.6$ nm NT of Figure 4.4, this gives E_{GAP} (theory) = 0.44 V, in reasonable agreement with the measured value 0.51V. Furthermore, the inferred band gaps presented in Table 4.1 scale accurately with the tube diameter (Figure 4.7). The good agreement between the theoretically expected values and the inferred values from measurement clearly demonstrate that the low bias I - V_{SD} curves for these diodes provide a direct measure of the band gap of the NT.

The inferred transmission coefficient $\mathfrak{S}_0 = 0.2$ indicates that the motion of carriers across the junction region and to the other contact is quite efficient. We note that there are two parts to this process. First, electrons or holes must traverse the ~ 1 micron depletion region. Second, when the carrier emerges on the other side, it must recombine or diffuse to the other contact approximately 1-2 microns away before it falls back down the large potential barrier it surmounted. It is useful to compare these length scales to those of competing mechanisms that would lead to the loss of charge carriers. Phonon scattering lengths in semiconducting NTs have been measured to be between 100 nm and 1 micron, depending on temperature and the energy of the electron (Zhou et al. 2005). The electron-hole recombination length is not known in NTs, but optical measurements in light-emitting NT devices show a recombination length on the scale of several microns (Freitag et al. 2004). Given that the length scales of these processes are on the same order, a transmission coefficient of $\mathfrak{S}_0 = 0.2$ seems quite reasonable.

The factor $n = 1.2$ is similar to that found by Lee et al. when fitting to the ideal diode equation at room temperature. Our results and analysis confirm explicitly this thermal activation form over a wide temperature range. The deviation from the ideal condition $n = 1$ could be the result of a number of effects. In standard diode theory, n takes on values between 1 and 2, 1

Table 4.1. Extracted parameters from the one-dimensional transport model

Summary of transport results					
	D (nm)	E_g (meV)	\mathfrak{F}_0	n ($V_g = 0$ V)	V_{BR} (T=200K)
Device 1	1.2 ± 0.3	620	0.3	1.2	7.3
Device 2	1.6 ± 0.3	510	0.2	1.2	5.9
Device 3	2.7 ± 0.3	300	0.1	1.8	5.1
Device 4	3.2 ± 0.3	250	0.3	1.5	4.9

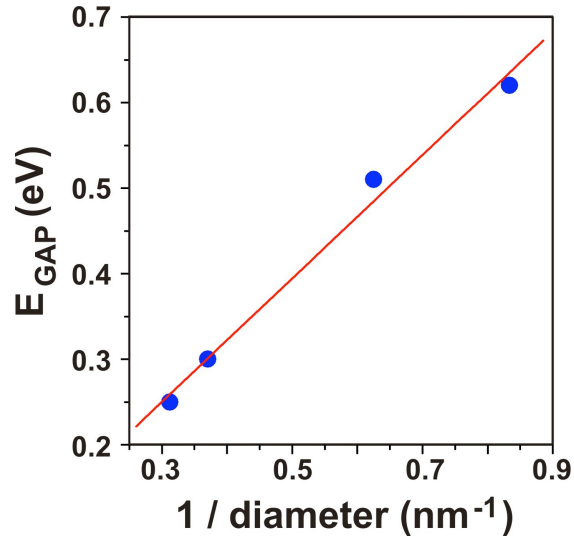


Figure 4.7. Band gap energy as a function of nanotube diameter extracted from the low temperature transport characteristics of several NT PN junctions.

being the limit of no recombination in the depletion region, and 2 being the limit of complete recombination. Alternately, disorder in the junction may make the bottleneck for transport somewhere in the depletion region, and there will be a lever arm relating the change in barrier height with applied voltage. Suspended NT PN junctions have been found to have $n = 1$ (Lee et al. 2006), which is consistent with both of the models above, since suspended tubes likely have less disorder and fewer recombination centers.

4.6 Reverse Bias and Diode Breakdown

The final section of this chapter discusses the reverse bias characteristics of the NT $p-i-n$ junction. In Figure 4.8a, we show the reverse bias $I-V_{SD}$ characteristics for a device with diameter $d = 1.2$ nm at varying temperatures. In Figure 4.8b, we show similar characteristics at constant temperature $T = 200$ K for devices with different diameters. To analyze the reverse bias data, we define a breakdown voltage V_{BR} as the voltage under reverse bias at which $R = V/I \sim 1\text{G}\Omega$. From the analysis of curves in Figure 4.8, we determine V_{BR} as a function of temperature and NT diameter (shown in Figure 4.8 insets). The breakdown voltage is in the range of 4 to 9 V for all of the devices measured. It grows with decreasing NT diameter and with decreasing temperature. In the breakdown region, the current rises approximately exponentially with bias: $I = A \exp(V/a)$, where a is typically 50-100 mV.

There are two main mechanisms for reverse bias breakdown in standard semiconductor diodes: interband (Zener) tunneling and avalanche breakdown (Sze 1981). We first consider Zener tunneling. The transmission probability for tunneling through the gap can be estimated using the WKB approximation (Leonard et al. 1999, Capaz et al. 2005)

$$\mathfrak{T} = \exp\left[-\frac{2}{\hbar} \int_0^{t/2} (2mEx)^{1/2} dx\right] = \exp\left[-\frac{4}{3\sqrt{2}\hbar} \frac{E_{GAP}^2}{v_F \epsilon}\right] \quad (4.3)$$

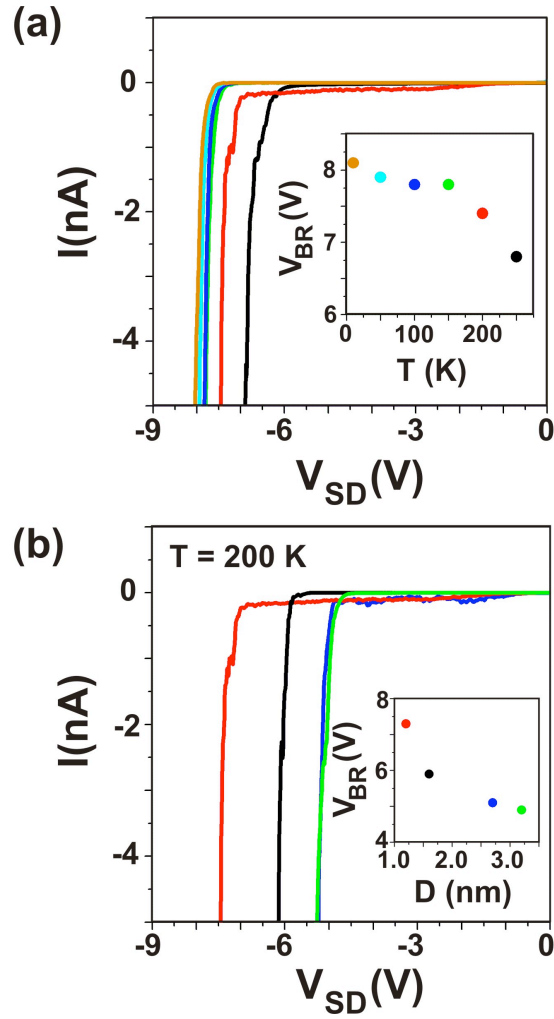


Figure 4.8. Reverse bias I - V_{SD} characteristics showing device breakdown at large reverse bias. **(a)** Reverse bias characteristics for a device of $d = 1.2$ nm at several temperatures. **Inset**, the breakdown voltage V_{BR} as a function of temperature for the same device. V_{BR} is defined as the voltage at which the resistance is ~ 1 GOhm. **(b)** Reverse bias characteristics at $T = 200$ K for devices of different diameters. **Inset**, V_{BR} plotted as a function of NT diameter.

where $\mathbf{E} = (E_g + V)/L$ is the electric field in the junction region (assuming for simplicity a constant electric field) and $t = E_g/\mathcal{E}$ is the distance that the electron must tunnel. Using Equation (4.3), we can predict the threshold voltage at which the junction resistance is 1 G Ω :

$$V_{BR}(Zener) \approx 75 \text{ V} (L[\text{mm}] / d[\text{nm}]^2) - E_{GAP} \quad (4.4)$$

In Figure 4.8, the experimentally measured values are smaller than those predicted by Equation (4.4) assuming $L \sim 1$ micron; a channel length $L \sim 100$ nm would bring the prediction more in line with the measured values. However, the diameter dependence is much weaker than predicted by Equation (4.4) and the measured inverse slopes $\alpha = dV/d(\ln I) = 50\text{-}100$ mV of the exponential turn-on are significantly smaller than those derived from Equation (4.3): $\alpha = V_{BR} / \ln(\mathcal{S}_{BR}) \approx V_{BR} / 15$. Zener breakdown voltages typically decrease with increasing temperature due to the change in the band gap with temperature. While this is in agreement with the data in Figure 4.8a, the magnitude of this effect in NTs is too small to explain the measured shifts (Capaz et al. 2005). For all these reasons, it is unlikely that the breakdown is by Zener tunneling in the bulk of the depletion region, although tunneling through imperfections or places where the electric field is high cannot be ruled out.

The second potential mechanism is avalanche breakdown. The electrons and holes in the intrinsic region accelerate in the electric field of the junction until they have enough energy to create a new electron-hole pair. Competing with this process is energy loss by phonon emission, which has been extensively studied in NTs both theoretically and experimentally (Zhou et al. 2005, Park et al. 2004, Pop et al. 2005, Yao et al. 2000). According to these studies, the spontaneous emission of large-energy ($\hbar\omega_o \sim 0.2$ eV) optic or band edge phonons occurs with a mean free path of $\ell \sim 30$ nm. In order for the energy gained by the electric field to exceed the energy lost by phonon emission, the voltage across the junction must be greater than:

$$V_{BR}(avalanche) > (\hbar\omega_o/e\ell)L = 8 \text{ V} \cdot L [\text{microns}] \quad (4.5)$$

This estimate is consistent with the data, assuming a junction width L of order of, but slightly smaller than, the 1 micron distance between the gate electrodes. An increase of the breakdown voltage with tube diameter is also expected since the electron or hole must accelerate to a larger energy, but a specific prediction requires detailed knowledge of all the relevant scattering rates. Not all of the data is consistent with avalanche behavior, however. In most avalanche diodes, V_{BR} increases as the temperature is raised, since raising the temperature increases phonon scattering.

While further studies are needed to unambiguously determine the breakdown mechanism in our devices, some progress in understanding avalanche multiplication in NTs has been made. Theoretical work by Perebeinos et al. (2006) determined the conditions under which multiplication will occur in NTs. By considering energy and momentum conservation in the NT band structure, they showed that higher subband carriers undergo multiplication more efficiently than lower subband carriers (Perebeinos et al. 2006). Liao et al. (2008) conducted a detailed series of measurements of avalanche breakdown behavior in NT field effect transistors and found that avalanche multiplication is very efficient and leads to remarkable current increase at internal electric fields of ~ 10 V/micron. Based on the theory by Perebeinos et al., they attribute efficient multiplication to carriers injected into higher subbands of the NT band structure. As will be discussed in the next chapter, higher subbands indeed play a significant role in the multiplication of electron-hole pairs in NTs.

4.7 Conclusion

In this chapter, we have shown that the nanotube PN junction exhibits the behavior expected for a nearly ideal one-dimensional diode over a wide range of temperatures. These measurements provide a direct measure of the band gap of the nanotube and the transmission probability through the junction region. The reverse bias breakdown happens at a voltage much larger than characteristic forward bias voltages and is a weak function of temperature and diameter. A substantial intrinsic region between the p- and n-type regions is necessary to see the good diode behavior; sharp PN junctions leak under both forward and reverse bias, likely due to

increased tunneling across the smaller depletion region. These results are crucial for evaluating the use of nanotubes for both bipolar and optoelectronic devices.

CHAPTER 5

MULTIPLE ELECTRON-HOLE PAIR GENERATION IN NANOTUBE PN JUNCTIONS

5.1 Introduction

The electronic properties of charge carriers in graphene sheets and carbon nanotubes exhibit striking similarities to relativistic elementary particles. As discussed in previous chapters, the linear dispersion and electron-hole-symmetric band structure of graphene provides a compelling analog to two-dimensional massless Dirac fermions (Saito et al. 1998, Novoselov et al. 2005, Katsnelson et al. 2006, Avouris et al. 2007, Ponomarenko et al. 2008). As in string theory, rolling up the graphene sheet to make a single-walled carbon nanotube (NT) generates numerous species of one-dimensional fermions whose energies are given by

$$\varepsilon_i(k) = \pm \sqrt{(m_i^* v_F)^2 + (\hbar k_{\parallel} v_F)^2} \quad (5.1)$$

where $v_F = 8 \times 10^5$ m / s is the Fermi velocity of graphene, \hbar is Planck's constant, $\hbar k_{\parallel}$ is the carrier momentum along the length of the nanotube and m_i^* is the effective mass of the i^{th} subband. In direct analogy to relativistic particle physics, both positive and negative energy solutions are allowed (electrons and holes) and the rest energy of the particles is given by $m_i^* v_F^2$, where v_F plays the role of the speed of light c . For a semiconducting NT, the band gap energy $E_{11} = 2m_1^* v_F^2$ is the energy required to generate an electron-hole pair, while higher subband energies such as $E_{22} = 2E_{11}$ correspond to excitations of more massive particles ($m_2^* = 2m_1^*$).

A remarkable prediction of relativistic quantum mechanics is the ability of high-energy particles to create particle-antiparticle pairs from the vacuum (Weinberg 1995). The occurrence of such a process depends strongly on the ratio of the interaction strength between electrons to their relativistic energies, and is quantified by the fine structure constant $\alpha = e^2 / 4\pi\epsilon_0 \hbar c \sim 1 / 137$, where e is the electron charge and ϵ_0 is the permittivity of vacuum. Interestingly, the small

Fermi velocity and low dielectric constant in NTs leads to an effective fine structure constant $\alpha = e^2 / 4\pi\epsilon\hbar v_F \sim 1$, suggesting that high-energy carriers may efficiently generate particle-antiparticle (electron-hole) pairs. Processes by which a high-energy charge carrier generates additional electron-hole pairs are potentially of great practical importance. Efficient generation of electron-hole pairs could lead to highly sensitive photodetectors (Hayden et al. 2006, Yang et al. 2006), electro-luminescent emitters (Misewich et al. 2003, Chen et al. 2005, Marty et al. 2006), and, particularly, improved-efficiency photovoltaics (Tian et al. 2007, Lee et al. 2005, Schaller et al. 2004). Multiple electron-hole (e-h) pair generation could theoretically improve the efficiency of photovoltaic solar cells beyond standard thermodynamic limits (Shockley and Queisser 1961). Recent optical experiments have suggested that such processes occur in semiconductor nanocrystals (Schaller et al. 2004, Ellingson et al. 2005, Kim et al. 2008, Schaller et al. 2005), but the interpretation of these results is controversial.

In this chapter, we describe optoelectronic measurements on the NT PN junctions described in Chapter 4. We measure the electronic characteristics of the PN junction at various temperatures and under focused laser illumination. Using scanning photocurrent microscopy, we measure the spatially sensitive optoelectronic response at the PN junction. At high photon energies and low temperatures, the I - V_{SD} characteristics reveal striking step-like behavior in reverse bias. These steps scale with the NT band gap and can be attributed to extremely efficient impact excitation. In this process, a single highly energetic charge carrier undergoes extremely efficient multiplication into several electron-hole pairs. The main results of this chapter were published in Gabor et al. (2009).

5.2 Scanning Photocurrent Microscopy and I - V_{SD} Characteristics

To measure the optoelectronic characteristics, NT PN junction devices are placed in the SPSM setup that combines electronic transport measurements at low temperature with spatially scanned laser illumination (Chapter 3). Figure 5.1b shows a spatially resolved photocurrent map achieved by recording the current I as a focused laser ($\lambda = 532$ nm) is scanned over the device at

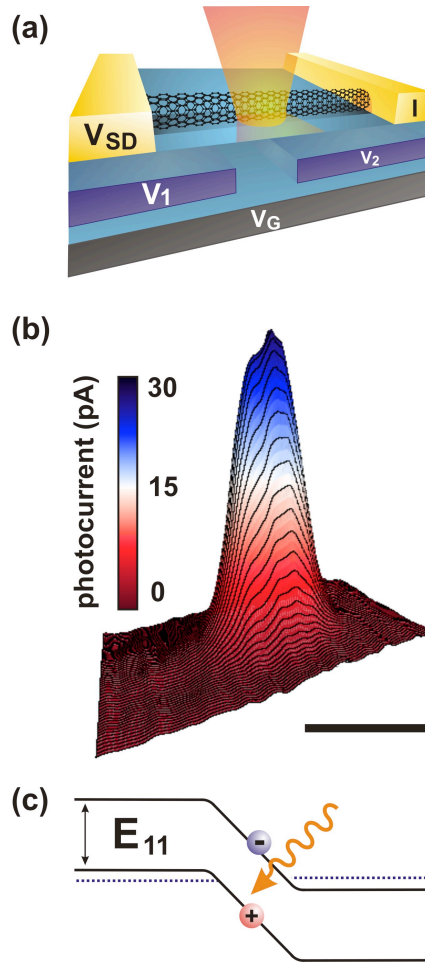


Figure 5.1. Device geometry and spatial photocurrent of the nanotube PN junction photodiode. **(a)** Experimental schematic of split gate device under focused optical illumination. **(b)** Spatially resolved photocurrent map at $T = 50$ K with continuous wave laser excitation $\lambda = 532$ nm and optical power density 25 W / cm² for a device of diameter $d = 1.8$ nm ($V_1 = -V_2 = -9.0$ V, $V_G = V_{SD} = 0.0$ V). Scale bar 1 micron. **(c)** Length-dependent potential energy diagram of PN junction at $V_{SD} = 0$ V. Dotted lines represent the electron Fermi energy in the p- and n- type regions of the device and E_{11} is the band gap energy.

a source-drain voltage $V_{SD} = 0$ V and $T = 50$ K. A photocurrent peak is observed at the location of the PN junction, with a full width at half maximum of ~ 700 nm perpendicular to the nanotube, consistent with the size of the excitation beam.

We next fix the position of the laser on the PN junction and measure I - V_{SD} characteristics at various photon energies and temperature $T = 60$ K for a device of diameter $d = 1.4$ nm (Figure 5.2). In the absence of light, the dark I - V_{SD} characteristic (black line) demonstrates ordinary PN junction transport behavior (Lee et al. 2004, Bosnick et al. 2006, Chapter 4): very small current in reverse bias and a threshold for turn-on in forward bias corresponding to the band gap of the NT. The illuminated I - V_{SD} characteristic at low photon energy ($E_{PHOTON} = 0.75$ eV, red curve) also exhibits a standard PN junction photo-response: constant photocurrent at reverse and moderate forward bias. At a forward bias equal to the band gap, the built-in potential disappears and the photocurrent goes to zero at the open circuit voltage ($V_{OC} = 0.43$ V), which gives the band gap energy $E_{GAP} = E_{II} \sim eV_{OC}$ in the PN junction (Sze 1981).

5.3 Optoelectronic I - V_{SD} Characteristics: Photon Energy and Diameter Dependence

In Figure 5.2, as the photon energy is increased, we observe a dramatically different response than that at low photon energies. The reverse-bias photocurrent increases with increasing photon energy and evolves into a series of steps with increasing reverse bias (Figure 5.2, $E_{PHOTON} = 1.24$ eV). We present similar results for a device of $V_{OC} = 0.3$ V in Figure 5.3. Photocurrent steps occur in reverse bias and the photocurrent increases linearly with optical power density. In the next sections of this chapter, we discuss the dependence of these current steps on source-drain bias, photon energy, and temperature.

The spacing of the steps in Figure 5.2 is $\Delta V_{STEP} \sim 0.4$ V, which is nearly the same as the open circuit voltage $V_{OC} = 0.43$ V. Similarly, in Figure 5.3a, photocurrent steps occur in intervals ΔV_{STEP} that are approximately equal to the open circuit voltage, $V_{OC} = 0.3$ V. To determine the spacing more accurately, we calculate the differential conductance $|dI / dV_{SD}|$ as a function of V_{SD} . Figure 5.3b shows $|dI / dV_{SD}|$ for NT devices of diameters 1.5 nm (orange), 2.0

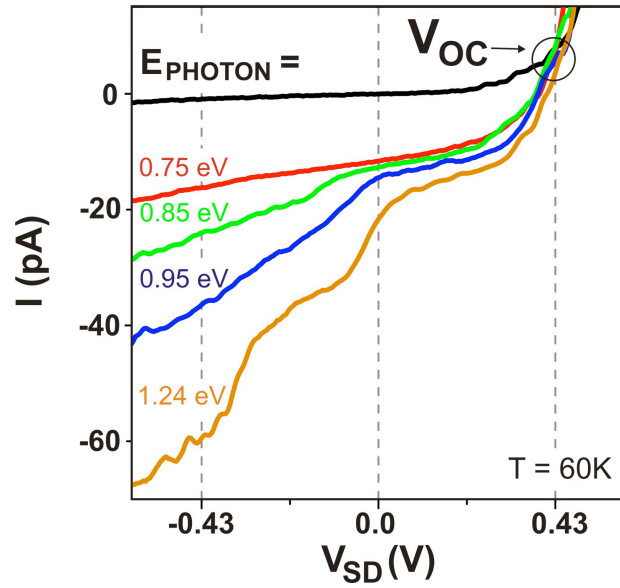


Figure 5.2. I - V_{SD} characteristics of the NT PN junction photodiode at $T = 60\text{ K}$ for NT with diameter $d = 1.4\text{ nm}$ at various photon energies (labeled), $V_1 = -V_2 = 7.5\text{ V}$, $V_G = 1.2\text{ V}$, and optical power density 25 W / cm^2 .

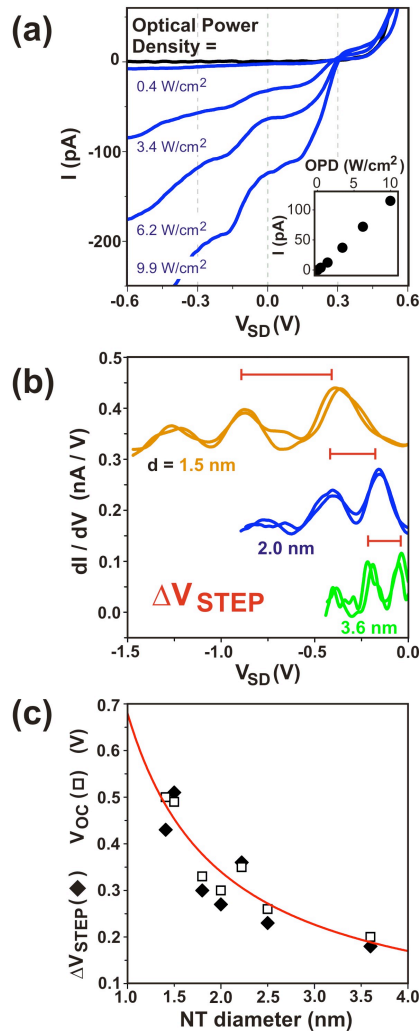


Figure 5.3. (a) I - V_{SD} characteristics at $T = 10$ K and $E_{PHOTON} = 0.79$ eV for a device of $d = 2.0$ nm and open circuit voltage $V_{OC} = 0.3$ V at several optical power densities (labeled) up to 10 W/cm². **Inset**, photocurrent at $V_{SD} = 0$ V vs. optical power density. (b) Reverse bias differential conductance $|dI / dV_{SD}|$ for devices with various diameters (labeled, offset by intervals of 1.5 nA/V) and multiple optical power densities (normalized and re-scaled for comparison to the bottom device by factors $\times 6$ (orange), $\times 3$ (blue), $\times 1$ (green)) at $\lambda = 1420$ nm (orange) and $\lambda = 1560$ nm (blue, green)). (c) ΔV_{STEP} and V_{OC} plotted against nanotube (NT) diameter for several devices.

nm (blue), and 3.6 nm (green). Conductance peaks, corresponding to photocurrent steps, occur at shorter V_{SD} intervals for devices of larger diameter. In Figure 5.3c, we plot V_{OC} and ΔV_{STEP} versus NT diameter for several devices. The photocurrent step intervals, ΔV_{STEP} scale inversely with NT diameter approximately as $\sim 0.66 [V\text{-nm}] / d$, shown as a solid line. This result is consistent with the dependence of the band gap energy on diameter d : $E_{11} \sim eV_{OC} \sim 0.7 [\text{eV}\text{-nm}] / d$. We conclude that the spacing ΔV_{STEP} of the photocurrent peaks is equal to the band gap E_{11} of the NT.

5.4 Photocurrent Spectroscopy and Temperature Dependence

Photocurrent spectroscopy measurements show that photocurrent steps occur only for photon energies $E_{PHOTON} > 2E_{11}$. In Figure 5.4a, we plot the photocurrent spectra for the device of Figure 5.2 at $V_{SD} = V_{OC} / 2$ (slight forward bias) and $V_{SD} = -V_{OC} / 2$ (slight reverse bias). At $E_{PHOTON} = 0.81 \text{ eV}$, we observe a narrow spectral peak. Upon normalizing the photon energy by eV_{OC} , we observe that the spectral peak occurs near $E_{PHOTON} \sim 2E_{11}$, which is consistent with optical absorption into the second subband, $E_{22} = 2E_{11}$. The extra photocurrent seen at high photon energy ($E_{PHOTON} > 2E_{11}$) corresponds directly to the photocurrent steps in the I - V_{SD} characteristics in Figure 5.2. In Figure 5.4b, we observe a similar response for a device of $V_{OC} = 0.45 \text{ V}$. From the photocurrent spectroscopy, we conclude that the photocurrent steps occur only under excitation of second subband electrons e_2 and holes h_2 .

The photocurrent steps also occur only at low temperatures. For the device used in Figure 5.4b, we show in Figure 5.5a the I - V_{SD} characteristics at various temperatures at $E_{PHOTON} = 0.95 \text{ eV}$ and $E_{PHOTON} = 0.76 \text{ eV}$ (above and below the spectral peak at $E_{PHOTON} \sim 2E_{11}$). At $E_{PHOTON} = 0.95 \text{ eV}$ ($E_{PHOTON} > 2E_{11}$), we observe a very strong temperature dependence and clear photocurrent steps below $T \sim 100 \text{ K}$ (Figure 5.5a top). At $E_{PHOTON} = 0.76 \text{ eV}$ ($E_{PHOTON} < 2E_{11}$), in contrast, the I - V_{SD} characteristics show very weak dependence on temperature, exhibiting no photocurrent steps (Figure 5.5a bottom). In Figure 5.5b, we plot the temperature dependence of the reverse ($V_{SD} = -V_{OC} / 2$) and forward ($V_{SD} = V_{OC} / 2$) bias photocurrent. For

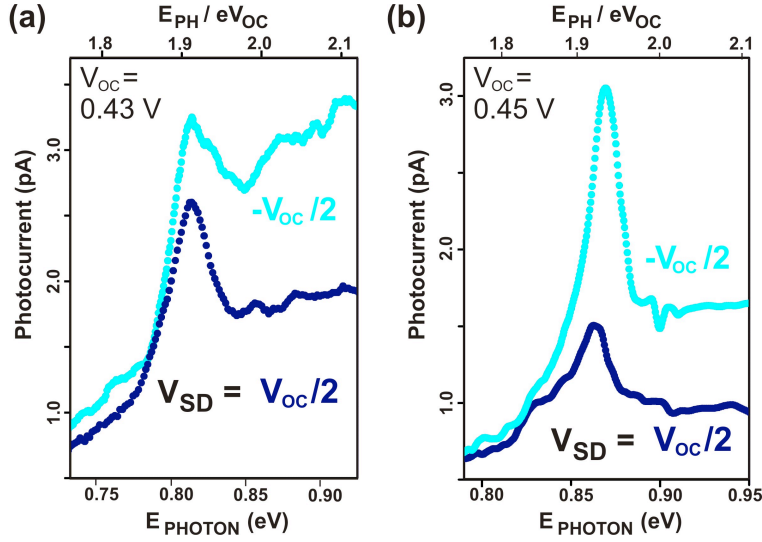


Figure 5.4. Photocurrent spectroscopy of the NT PN junction. **(a)** Photocurrent spectra for device of Figure 5.2 measured at $V_{SD} = V_{OC} / 2 = 0.225$ V (navy blue), and $V_{SD} = -V_{OC} / 2 = -0.225$ V (cyan), OPD = $3 \text{ W} / \text{cm}^2$. Top axis normalized by eV_{OC} . **(b)** Photocurrent spectra for another device ($d = 1.7$ nm, $V_{OC} = 0.45$ V, $V_1 = -V_2 = 6.0$ V, $V_G = 1.5$ V, $T = 49$ K), measured at $V_{SD} = V_{OC} / 2 = 0.225$ V (navy blue), and $V_{SD} = -V_{OC} / 2 = -0.225$ V (cyan), OPD = $3 \text{ W} / \text{cm}^2$. Top axis normalized by eV_{OC} .

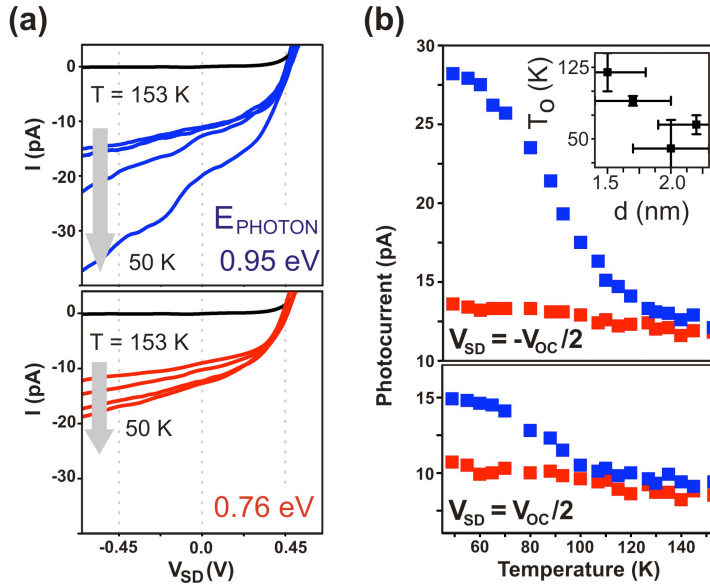


Figure 5.5. (a) **top**, I - V_{SD} characteristics for the device in figure 5.4b measured at photon energy $E_{PHOTON} = 0.95$ eV (blue) at various temperatures (descending in direction of arrow $T = 153, 127, 107, 50$ K), $OPD = 25$ W/cm². (a) **bottom**, I - V_{SD} characteristics measured for the same device at photon energy $E_{PHOTON} = 0.76$ eV (red) over the same temperature range. (b) **top**, temperature dependence of reverse bias ($V_{SD} = -V_{OC} / 2 = -0.225$ V) photocurrent at various temperatures for photon energies $E_{PHOTON} = 0.76$ eV (red) and $E_{PHOTON} = 0.95$ eV (blue). (b) **bottom**, temperature dependence of forward bias photocurrent ($V_{SD} = +V_{OC} / 2 = 0.225$ V). (b) **top inset**, Photocurrent step onset temperature T_0 vs. diameter for several devices.

$E_{PHOTON} > 2E_{11}$, the reverse bias photocurrent (Figure 5.5b top) doubles at low temperature and the forward bias photocurrent shows a similar, significant increase. By extracting the inflection point of the reverse bias data, we assign an onset temperature of $T_0 = 90$ K, below which photocurrent steps occur. We also measured the onset temperature for several devices (Figure 5.5b inset) and observe that T_0 decreases with diameter. Thus, these steps occur only for photon energies larger than E_{22} and below a characteristic temperature that depends on the NT diameter.

5.5 Model: Extremely Efficient Impact Excitation

We attribute the photocurrent steps to highly efficient electron-hole (e-h) pair creation by high-energy charge carriers in the second NT subband. In the e-h generation process requiring the lowest excess energy, the excess rest mass energy of the second subband carriers ($m_2^* v_F^2$) is combined with the kinetic energy of the electric field to create an e_1 carrier plus electron-hole pairs (Figure 5.6):

$$e_2 + K_e(x) \rightarrow e_1 + n(e_1 + h_1) \quad (5.2a)$$

and, equivalently for holes:

$$h_2 + K_h(x) \rightarrow h_1 + n(e_1 + h_1). \quad (5.2b)$$

The integer $n = 1, 2, 3, \dots$ indicates the number of e-h pairs produced in the final state of the generation process. The intermediate states of Equation (5.2) may involve an e_2 carrier undergoing several impact excitation events or a single relaxation event that results in numerous e-h pairs. The kinetic energy available to electrons (K_e) and holes (K_h) created at a position x along the PN junction of length L is given by:

$$K_e(x) = e\phi(x) \quad (5.3a)$$

$$K_h(x) = e\phi_0 - e\phi(x) \quad (5.3b)$$

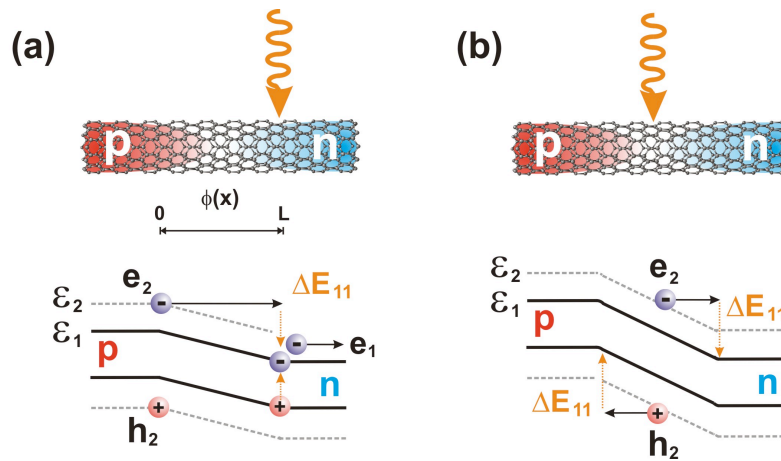


Figure 5.6. Model: Impact excitation in the NT PN junction. **(a)** Electronic potential energy diagram for the PN junction at $V_{SD} = V_{OC} / 2$ V with electrons and holes generated at the edges of the junction, $x = 0$ (top) and $x = L$ (not shown). ε_1 and ε_2 label the first and second subbands. **(b)** Electronic energy diagram for the PN junction at $V_{SD} = 0$ V with electrons and holes generated at the center of the junction. For clarity, the electron-hole pairs generated by impact excitation are not shown.

where $e\phi(x)$ is the electric potential energy and $e\phi_0 = e\phi(L) - e\phi(0) = E_{II} - eV_{SD}$ is the total potential energy drop across the PN junction. The potential energy drop can be tuned by changing V_{SD} . At the open circuit voltage, $V_{SD} = V_{OC} \sim E_{II} / e$, the total potential energy drop is zero, while at $V_{SD} = 0$, the total potential energy available along the entire junction is $E_{II} = E_{GAP}$.

This model makes a number of predictions that can be compared to experiment. First, the amount of kinetic energy gained by a carrier in the PN junction depends strongly on its initial location. As shown in the schematic of Figure 5.6a, for carriers excited at the edge of the junction, either the electron *or* the hole picks up the entire potential energy of the junction while the other is unaffected. For the electron and hole created at the center, each picks up only half of the junction's potential energy (Figure 5.6b). The threshold for impact excitation will thus depend on the location of the photo-excitation.

5.6 Spatial Dependence of Photocurrent in the PN Junction

To test the predictions of the impact excitation model, we use scanning photocurrent microscopy measurements. In Figure 5.7, we plot photocurrent profiles for a device of $V_{OC} = 0.45$ V taken by scanning the laser ($\lambda = 676$ nm) along the length of the nanotube at various V_{SD} values. At $V_{SD} = 0.35$ V, we observe a flat photocurrent profile that extends across the entire PN junction with a constant value of ~ 10 pA. Such standard behavior does not include the effects of impact excitation. At $V_{SD} = V_{OC} / 2 = 0.225$ V, the photocurrent profile exhibits a double-peaked structure with photocurrent maxima occurring at the edges of the PN junction, corresponding to the case shown in Figure 5.6a in which electrons and holes undergo impact excitation. When the bias voltage reaches $V_{SD} = 0$ V, an additional sharp increase occurs at the center of the device, corresponding to Figure 5.6b. In reverse bias, the photocurrent peaks at the edges catch up to the center peak (at $V_{SD} = -V_{OC}$) until finally, at high reverse bias the center peak again dominates over the side peaks.

To explore this spatial dependence in detail, we first fixed the laser on the edge of the PN junction (Figure 5.8a). The first photocurrent step occurs in forward bias at $V_{SD} \sim 0.25$ V. The

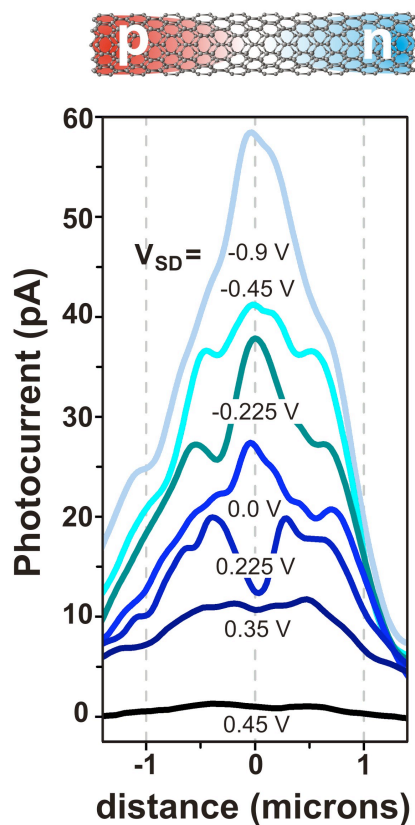


Figure 5.7. Scanning photocurrent line profiles of the NT PN junction. Profiles for a device of $V_{OC} = 0.45$ V at $T = 75$ K as a function of V_{SD} (values labeled). The laser ($\lambda = 676$ nm) is scanned along the length of the nanotube (top schematic) and photocurrent is measured simultaneously. The central peak appearing at $V_{SD} = 0$ V corresponds to the process shown in Figure 5.6b while the peaks at the edges of the junction are due to the processes shown in Figure 5.6a, and are suppressed at elevated temperatures.

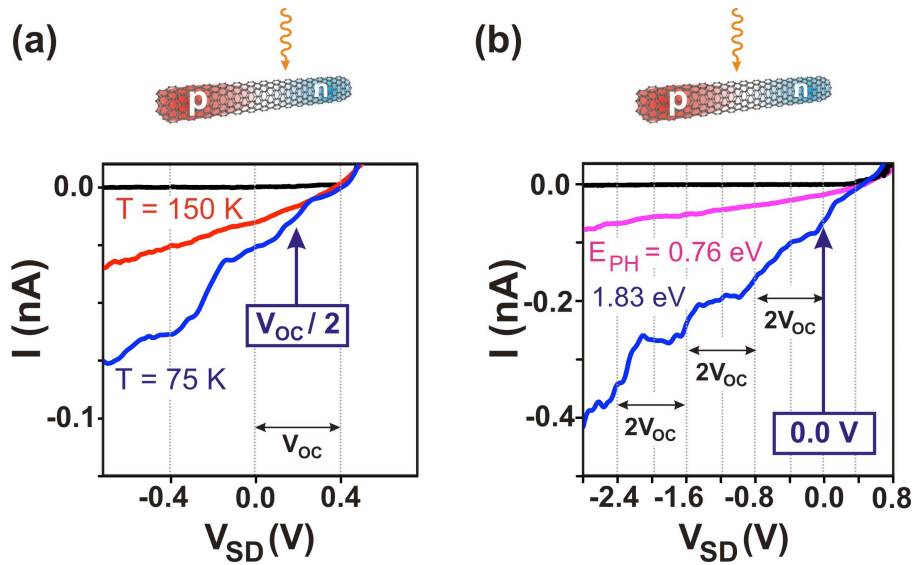


Figure 5.8. (a) I - V_{SD} characteristics with the laser fixed at the *edge* of the device at various temperatures (labeled). Blue box labels the onset voltage for the first photocurrent step and dotted lines mark the voltage spacing V_{oc} . (b) I - V_{SD} characteristics with the laser fixed at the center of the device at various photon energies (labeled).

first photocurrent step in forward bias corresponds to the edge peaks of the double-peaked structure in the spatial photocurrent profile at low temperature (Figure 5.7 $V_{SD} = 0.225$ V). The second step is observed at $V_{SD} \sim -0.20$ V, with a spacing between photocurrent steps $\Delta V_{STEP} \sim V_{OC} = E_{II}$.

The photocurrent voltage threshold for the first step highlights a key feature of the e-h generation process. When the laser is fixed at the edge of the PN junction, electron-hole pair creation first occurs in forward bias at $V_{SD} = \frac{1}{2} E_{II} / e = V_{OC} / 2$. The electric field need only provide kinetic energy of $\frac{1}{2} E_{II}$ while the remaining energy is provided by the conversion of rest mass energy (or equivalently by excess subband energy), as indicated in Equation (5.2).

For comparison, we next show I - V_{SD} characteristics with the laser fixed on the center of the PN junction (Figure 5.8b). Because electrons e_2 and holes h_2 start at the center of the PN junction and gain only half of the electric potential energy, the applied voltage V_{SD} threshold for electron-hole pair production is doubled. Indeed, we observe the first photocurrent step near $V_{SD} = 0$ V and additional steps in reverse bias at V_{SD} intervals of $2V_{OC}$. At higher kinetic energies, additional e-h pair production requires an additional combined energy of $2E_{II}$ from the electric field (E_{II} for each of the electron and hole) and leads to photocurrent steps at larger voltage intervals of $2V_{OC}$. This response is consistent with the e-h pair production process of Equation (5.2): the onset voltage threshold and voltage spacing for additional steps depend strongly on the initial location of the photo-excited carrier.

5.7 Discussion and Comparison to Theoretical and Experimental Work

The impact excitation process $e_2 + K_e \rightarrow e_1 + n(e_1 + h_1)$ differs strongly from impact ionization observed in traditional semiconductors in two important ways. First, no avalanche breakdown behavior is observed here because hot e_2 carriers create e_1 carriers, which do not undergo additional multiplication at low reverse bias. Second, the process observed here is extremely efficient, occurring as soon as it is energetically allowed. In standard semiconductors, competing loss mechanisms restrict impact excitation to extremely large biases (Sze 1981).

The extremely high efficiency of the $e_2 + K_e \rightarrow e_1 + n(e_1 + h_1)$ process is a surprising result. Normally, relaxation mechanisms, such as optical phonon emission, are very efficient for relaxing hot carriers, including those in the first subband of NTs (Pop et al. 2005, Park et al. 2004, Yao et al. 2000). We do not know why the $e_2 \rightarrow e_1$ process reported here is different. Note, however, that other phonons may be important in reducing e-h pair generation at elevated temperatures. The thermal energy at the onset temperature is comparable to the radial breathing mode (RBM) energy $E_{RBM} \sim 7meV / d[nm]$ (Saito et al. 1998, Avouris et al. 2007) and other low-energy radial phonons. Indeed, recent optical measurements of the relaxation process $E_{22} \rightarrow E_{11}$ have suggested strong exciton-phonon coupling to the NT radial breathing mode at room temperature (Manzoni et al. 2005). Although the low temperature onset of impact excitation is comparable to the freeze-out of RBM phonons ($T < E_{RBM} / k_B \sim 80$ K for a 1 nm diameter NT), other processes may be responsible.

While our results differ strongly from previous theory (Chapter 2) and experiment in NTs, recent additional work has begun to investigate the details of the electron-hole pair generation process. Previous to our work (and discussed in Chapters 2 and 4) Perebeinos et al (2006) calculated that single-particle impact excitation in NTs should be highly efficient, but only in the third subband E_{33} and higher because of momentum conservation transverse to the NT axis. We observed impact excitation in the second subband E_{22} , suggesting that either other carriers or phonons are involved to conserve momentum. Baer et al. (2010) reconciled the difference between our results and the theory of Perebeinos by proposing an important variation on the impact excitation model. In their model, the initial electron-hole excitation above the second subband ε_2 relaxes very quickly into an ε_1 electron (hole) and an ε_3 hole (electron). Interactions of the ε_3 carriers with the diode field leads to the efficient impact excitation process described by Perebeinos et al.

$$e_3^4 \rightarrow e_2^2 + e_1^1 + h_1^1. \quad (5.4)$$

In addition, Baer et al. extended this model to calculate carrier scattering rates and the explicit temperature dependence of the electron-hole pair generation process, which shows good agreement with experiments. While the microscopic details of Equation (5.4) disagree with the process proposed in Equation (5.2), both processes lead to the same experimental finding: extra photocurrent above the photon threshold of $2E_{GAP}$.

In addition to theoretical work, earlier experiments on NTs attributed bright electroluminescence (Misewich et al. 2003, Chen et al. 2005, Marty et al. 2006) and avalanche breakdown (Liao et al. 2008) to electron-hole generation by impact excitation, but as with traditional semiconductors, these processes were only observed at large biases, and the importance of subband index was not discussed. More recently, transient absorption spectroscopy measurements on chemically isolated semiconducting (6,5) NTs were used to observe multiple exciton generation (MEG) (Wang et al. 2010). In these measurements, absorption of single photons with energies corresponding to three times the band gap E_{GAP} resulted in an exciton generation efficiency of 130%. Consistent with our measurements, at photon energies above twice the band gap, Wang et al. also observed an increase in exciton generation efficiency even at room temperature. In order to understand the details of this process, further experiments that probe the number of multiplied carriers (charge sensitive measurements such as shot noise) and their initial energies are needed.

5.8 Conclusion

The e-h pair creation process discussed in this chapter may make possible increased power conversion efficiency in future photovoltaic devices. The standard limit of photovoltaic efficiency, first established by Shockley and Queisser (1961), is set by the conversion of a single photon into a single e-h pair. In the NT PN junction, a single photon with energy $E_{PHOTON} > E_{22}$ is converted into multiple e-h pairs, leading to enhanced photocurrent and increased efficiency. Evidence for a related process, known as multiple exciton generation (MEG) (Schaller et al.

2004, Ellingson et al. 2005, Kim et al. 2008, Schaller et al. 2005), has been observed in various semiconductor nanocrystals, but these observations remain controversial, and improved photovoltaic device behavior has not been demonstrated. The results presented here clearly show that multiple e-h pairs can be generated and collected in a nanotube PN junction. Although implementation of devices exploiting e-h pair generation into photovoltaic cells will require substantial future effort, the process observed here has significant implications for such technology and represents a very important step towards ultra-efficient photovoltaic devices with power conversion efficiency exceeding the Shockley-Queisser limit.

CHAPTER 6

THE ESCAPE OF ELECTRONS AND HOLES FROM THE NANOTUBE PN JUNCTION

6.1 Introduction

Highly efficient photovoltaic and photo-detector devices, which make use of multiple electron-hole pair generation from a single photon (Gabor et al. 2009, Wang et al. 2010, Schaller et al. 2004, Ellingson et al. 2005), require comprehensive understanding of charge carrier dynamics and their role in optoelectronic response. In order to study dynamics in nanoscale systems such as carbon nanotubes (NTs) and nanocrystal quantum dots, numerous measurements have been developed to probe the relevant time scales of electron motion in ensembles of these novel materials. In NTs, the time scale over which carrier interactions occur may range from 10^{-14} second for intrasubband relaxation (Manzoni et al. 2005) to greater than 10^{-9} to 10^{-7} second for radiative recombination (Wang et al. 2004, Hagen et al. 2005, Berger et al. 2007, Pecht et al. 2011). However, no measurements have combined ultrafast optical and electronic techniques to probe the carrier dynamics and interactions in *individual* nanotube optoelectronic devices. While optical probes measure either the creation of electron hole pairs/excitons (absorption) or their relaxation (emission), photocurrent measurements probe a different quantity, the photoexcited carriers that escape the junction as separate electrons and holes. This time scale is not easily accessible from optical measurements, but is key for understanding the behavior of photovoltaics.

In this chapter, we present the first ultrafast photocurrent measurements of an individual NT optoelectronic device that incorporates sub-picosecond laser pulses. Using our technique, we directly probe the transit of electrons and holes through a NT p-i-n junction in the time domain, finding that carriers in the first subband (of effective mass m_1^*) escape the device in half the time as carriers in the second subband ($m_2^* = 2m_1^*$). Our measurements indicate that carrier escape is

diffusive in forward bias and, as the escape time decreases, approaches ballistic transport in reverse bias.

6.2 Measuring Photocurrent at Ultrafast Time Scales

Figure 6.1a shows the experimental schematic for measuring photocurrent at ultrafast time scales. A femtosecond Ti:Sapphire laser (repetition rate $f = 75$ MHz and pulse width < 200 fs) or an optical parametric oscillator (same repetition rate and pulse width < 300 fs), with respective wavelength ranges of 780-1000 nm and 1200-1600 nm, is used to photo-excite a nanotube p-i-n junction, described in previous chapters. The beam is focused through a microscope objective onto the NT sample in an optical cryostat at $T = 40$ K. The beam diameter is characterized using scanning photocurrent microscopy (Gabor et al. 2009, Chapter 5) and exhibits diffraction-limited Gaussian intensity distribution at the wavelengths used. We measure photocurrent response to single pulses or as a function of the time delay between two pulses. This is accomplished by splitting the output laser beam into a reference and delay beam separated by a time interval Δt . This temporal separation can be tuned by varying the optical path of the delay beam.

A schematic of the nanotube device is shown in Figure 6.1b, as described in previous chapters and in Gabor et al. (2009), and Bosnick et al. (2006). Gate electrodes (V_1 , V_2 , and bottom gate V_G) beneath a nanotube form a p-i-n junction with a source-drain contact distance of 3 microns. The I - V_{SD} curve of the device shows a diode characteristic (Figure 6.1b) when the split gate voltages V_1 and V_2 are of opposite polarity (Bosnick et al. 2006, Chapter 4). The turn-on voltage gives an approximate measure of the bandgap $V_{OC} = E_{GAP}/e = E_{11}/e$ where e is the elementary charge, and standard photocurrent spectroscopy measurements (Figure 6.1c) can be used to measure the energy E_{22} of the second subband (Wang et al. 2010, Freitag et al. 2003, Lee et al. 2007). For the device shown, referred to as device 1, these are found to be $E_{11} = 0.48$ eV and $E_{22} = 0.95$ eV. During the measurement, the source-drain voltage V_{SD} is varied while all gate voltages remain fixed to maintain a p-i-n configuration (see Chapter 4).

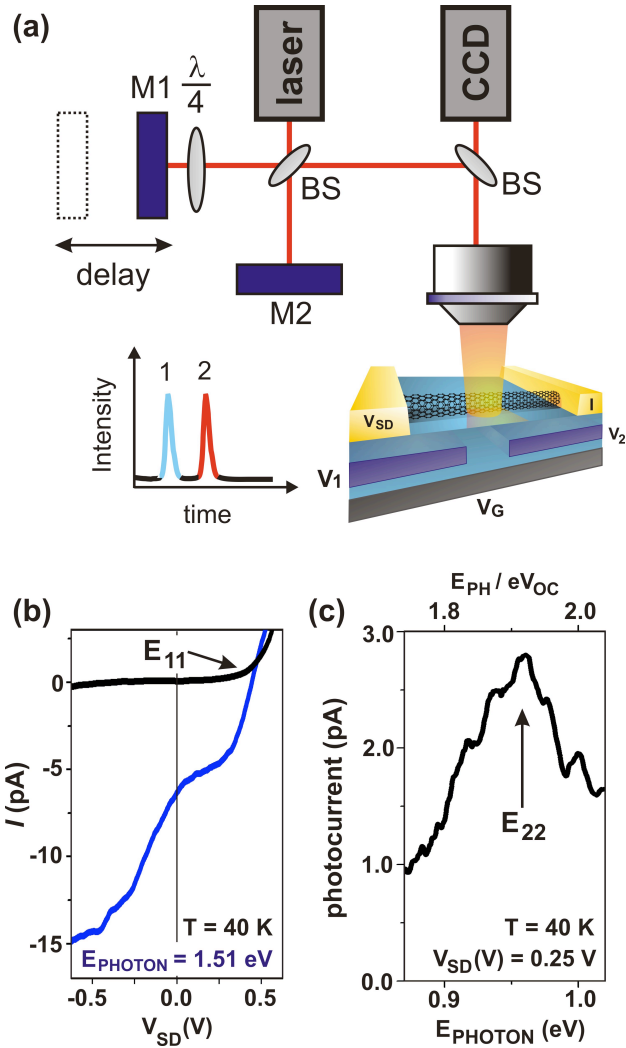


Figure 6.1. Experimental apparatus and photocurrent characteristics of the NT p-i-n photodiode. **(a)** Experimental apparatus: M1 translating mirror, M2 fixed mirror, BS beamsplitter. **(b)** I - V_{SD} characteristics at $T = 40$ K and $E_{PH} = 1.51$ eV, for device 1 with open circuit voltage $V_{OC} = E_{11}/e = 0.48$ V, $V_1 = -8$ V, $V_2 = 8$ V, $V_G = 1$ V. **(c)** Photocurrent vs. photon energy at $V_{SD} = 0.25$ V. All other parameters same as in **(a)**. The top axis has been divided by V_{OC} to assign the E_{22} peak.

6.3 Single Pulse Photocurrent: Sublinear Behavior

We first measure the low temperature photocurrent at the p-i-n junction due to a single optical pulse train (at $f = 75$ MHz) as a function of the excitation intensity n (number of photons per pulse / cm^2). Figure 6.2 shows photocurrent vs. intensity at $V_{SD} = 0$ V for device 1. We normalize the photocurrent data by the current value at which one carrier is generated per pulse (inset Figure 6.2a): $I = ef \sim 12$ pA. The photocurrent is linear for $I/ef < 1$ but becomes sublinear above $I/ef > 1$. The sublinear behavior can be approximately described as $I \sim n^{0.3}$ (Figure 6.2b).

The data of Figure 6.2 indicate that when multiple excitations dwell simultaneously in the junction, they strongly reduce the photocurrent response, likely due to electron-hole recombination. We can use this sublinearity of the photocurrent vs. intensity to probe the relevant time scale during which photo-excited excitations reside in the junction before escaping. In other words, how long must we wait before the junction is again empty? At zero time delay, two overlapping pulses will drive the photocurrent into strong sublinearity, while at long time delays the photocurrent will respond as though the pulses are independent, producing a larger current. The crossover between these two behaviors yields the escape time from the junction.

6.4 Double Pulse Photocurrent: V_{SD} Dependence

Figure 6.3a shows the double pulse photocurrent measured at $V_{SD} = 0$ V and $E_{PHOTON} = 1.51$ eV for the same device as in Figure 6.2. In Figure 6.3a, as intensity increases, we observe a photocurrent dip near $\Delta t = 0$ (when the two pulses overlap). The photocurrent dip is symmetric at positive and negative time delay and has a temporal width of ~ 400 fs at low intensities (experimental detection limit) and saturates to ~ 1 ps at high intensities.

We normalize the high intensity photocurrent near $t = 0$ (Figure 6.3b) and observe an exponential dependence vs. time delay with a characteristic decay time constant $\tau = 0.8$ ps at $V_{SD} = 0$ V. In the remaining sections, we discuss the dependence of the double pulse photocurrent decay time on source drain bias and photon energy.

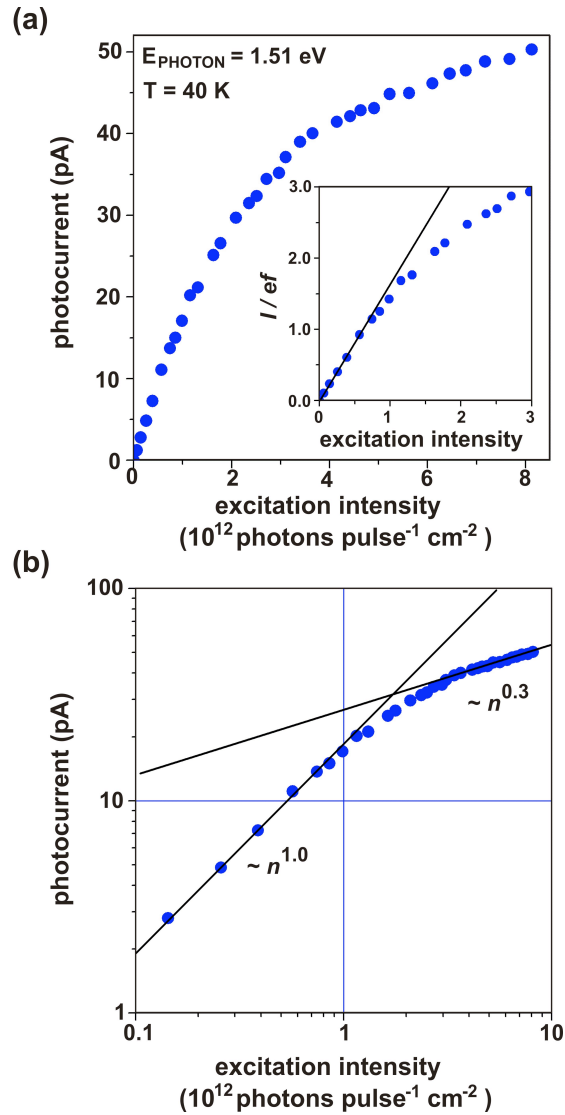


Figure 6.2. Single pulse photocurrent of the NT p-i-n photodiode. **(a)** Single pulse photocurrent vs. optical intensity at $T = 40$ K, $E_{PH} = 1.51$ eV and $V_{SD} = 0$ V for device 1. **Inset**, single pulse photocurrent divided by the elementary charge e and the repetition rate of the laser f vs. optical intensity. **(b)** Same data as **(a)** in log-log scale.

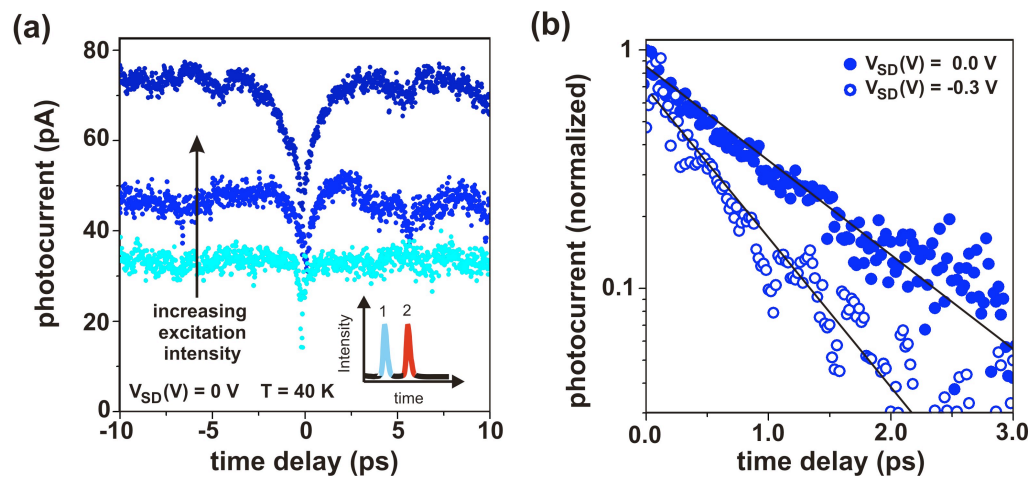


Figure 6.3. Double pulse photocurrent of the NT p-i-n photodiode. **(a)** Photocurrent vs. time delay between two pulses at $V_{SD} = 0 V$ at increasing intensities ($n = 5, 11,$ and 26×10^{12} photons per pulse/cm² from top to bottom) for the same device and conditions as Fig. 2. **(b)** Normalized photocurrent vs. time delay at $V_{SD} = 0 V$ (solid circles) and $V_{SD} = -0.3 V$ (open circles).

Figure 6.3b compares the normalized photocurrent vs. time delay at $V_{SD} = 0$ V and $V_{SD} = -0.3$ V. As the device goes from zero bias into reverse bias, the characteristic decay time τ decreases. We extract the characteristic decay constant at many V_{SD} values and plot them in Figure 6.4. In reverse bias, the decay time remains constant $\tau_0 \sim 0.5$ ps (labeled with a solid blue line). As V_{SD} approaches the open circuit voltage ($V_{OC} = 0.48$ V), the decay constant τ increases rapidly to $\tau = 1.4$ ps at $V_{SD} = 0.15$ V. Due to the decrease of photocurrent as V_{SD} approaches V_{OC} , characteristic time constants cannot be extracted close to V_{OC} . In the inset to Figure 6.4, we plot the inverse decay time $1/\tau$ as a function of V_{SD} . Importantly, the inverse decay time scales linearly with V_{SD} with a negative slope of $|s| = 2.3$ (V-ps) $^{-1}$ and extrapolates to an intercept of $V_{SD} = 0.45$ V as $1/\tau$ approaches zero.

6.5 Model: The Escape Time of Electrons and Holes From the PN Junction

The V_{SD} dependence of the decay time suggests that τ is set by the escape of electrons and holes out of the p-i-n junction. After optical excitation, electrons and holes are separated in the built-in electric field \mathbf{E} and accelerate towards the device contacts (Figure 6.5). As the electric field increases (moving from the flat band condition at the open circuit voltage into reverse bias), the charge carriers escape more quickly.

One model to describe this behavior is diffusive transport (see Chapter 1). During their escape from the junction, electrons and holes generated at the center of the device must travel a distance L with an electric-field dependent drift velocity $v_D = \mu\mathbf{E}$ where μ is the mobility. From the velocity, we get an expression for the escape time of electrons and holes out of the junction

$$\tau = \frac{2L^2}{\mu(V_{OC} - V_{SD})}. \quad (6.1)$$

Here, $\mathbf{E} = V/L$ is the electric field resulting from a voltage V applied over a distance L . The total applied voltage between p- and n-type regions is $V = (V_{OC} - V_{SD})/2 = (E_{GAP}/e - V_{SD})/2$, and L is

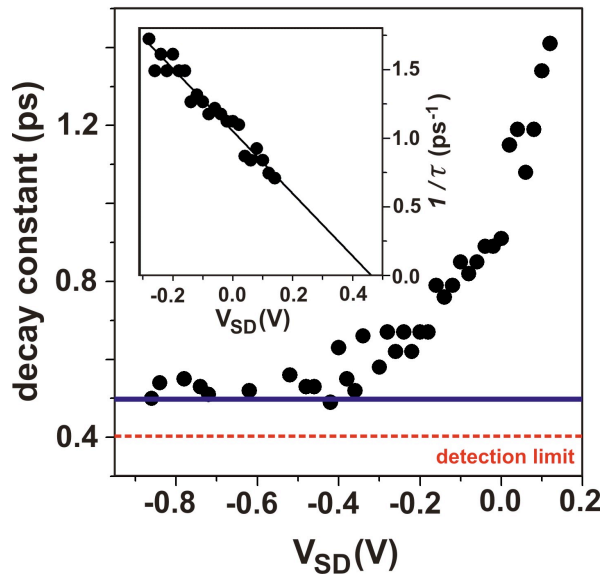


Figure 6.4. Extracted decay constant vs. V_{SD} . The red dashed line corresponds to the experimental resolution limit and the blue solid line labels $\tau_0 = 0.5$ ps. **Inset**, same data plotted as inverse decay constant $1/\tau$ vs. V_{SD} . The high reverse bias decay constant data is not shown in the inset.

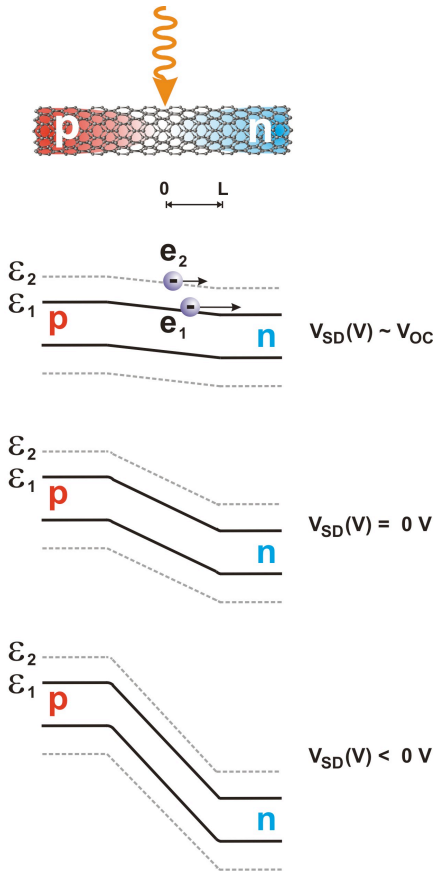


Figure 6.5. Schematic of the escape time model for electrons and holes in the PN junction. Electrons (and holes, not shown) photo-excited at the center of the device travel a distance L to escape the junction. When $V_{SD} \sim V_{OC}$, the built-in electric field is smallest, but as V_{SD} is increased in reverse bias, the electric field increases. The carrier transport follows an electric-field dependent velocity as electrons and holes exit the device.

half the length of the intrinsic region of the device since electrons and holes are generated at the center.

Comparing Equation (6.1) to our data, we see that the linear fit in the inset of Figure 6.4 indeed extrapolates to the open circuit voltage $V_{OC} \sim 0.48$ V which gives the band gap energy $E_{11} \sim 0.48$ eV. We can measure the length of the intrinsic region using scanning photocurrent microscopy and find a total length of ~ 1 μm for this device. Combining half this length $L \sim 0.5$ μm with the slope from Figure 6.4, we estimate the mobility in the *intrinsic* region of the p-i-n junction: $\mu = s2L^2 = 2(2.3 \text{ (V-ps)}^{-1})(0.5 \text{ } \mu\text{m})^2 \sim 1 \text{ } \mu\text{m}^2/\text{V-ps} \sim 10^4 \text{ cm}^2/\text{V-s}$, which is comparable to mobility values measured in high-mobility NT devices (Javey et al. 2003, Mann et al. 2003, Javey et al. 2004). We can also establish the upper limit of the scattering mean free path length of carriers as they transit the junction: $L_{MFP} \leq v_F \tau_S = v_F \mu m_2^* / e = \mu E_{22} / 2e v_F \sim 0.5 \text{ } \mu\text{m}$, where τ_S is the average time between scattering events, v_F is the Fermi velocity, and $m_2^* = E_{22} / 2v_F^2$ is the second subband effective mass (Yao et al. 2000, Chapter 2). This scattering length is comparable to the intrinsic region length, indicating that transport is at the border between diffusive and ballistic. It is slightly larger than the scattering length of high-energy ($\epsilon_{OP} \sim 0.2$ eV) optical phonons (Yao et al. 2000, Park et al. 2004, Zhou et al. 2005, Pop et al. 2005, Liao et al. 2008), the emission of which occurs with mean free path $L_{OP} \sim 100$ nm in semiconducting nanotubes (Liao et al. 2008).

We can also compare the results to a ballistic carrier model in the p-i-n junction. In NTs, carrier energies are given by a hyperbolic band structure in which the upper limit to the velocity of electrons and holes is the Fermi velocity $v_F \sim 0.8$ $\mu\text{m/ps}$ (Javey et al. 2004, Zhou et al. 2005, Saito, Dresselhaus, and Dresselhaus 1998, Avouris et al. 2010). In an electric field, ballistic transport is analogous to a relativistic electron in a static field limited by the speed of light. In the low-energy limit, the escape time varies inversely with $V_{SD}^{-1/2}$, analogous to a classical ballistic particle. This is not observed in Figure 6.4 and so rules out purely ballistic transport in forward bias.

One prediction of the diffusive model is that the escape time should vary in different subbands, since the mobility is inversely proportional to effective mass of charge carriers. In NTs, the effective mass m^* of the second subband electrons and holes is twice that of first subband carriers ($m_2^* = 2m_1^*$) (Zhou et al. 2005, Saito, Dresselhaus, and Dresselhaus 1998, Avouris et al. 2010). Due to the ratio of effective mass, the mobility μ (proportional to $1/m^*$) in the first subband should be twice that in the second subband ϵ_2 . Including this with Equation (6.1) leads to an important experimental consequence: Carriers that are optically excited into the second subband (with effective mass $m_2^* = 2m_1^*$) should take longer than first subband carriers to accelerate out of the junction, assuming the scattering times are the same and that relaxation occurs via free carrier scattering (Perebeinos et al. 2006). Using ultrafast photocurrent measurements, we can probe the escape time of electrons and holes above and below E_{22} and test this hypothesis.

6.6 Double Pulse Photocurrent: Photon Energy Dependence

Figure 6.6 shows measurements of the double pulse photocurrent vs. time delay in forward bias above and below E_{22} for device 2. We observe that the normalized photocurrent above E_{22} (blue data) decays with a time constant of $\tau_2 \sim 2.2$ ps, while the photocurrent below E_{22} (red data) decays within $\tau_1 \sim 1.3$ ps. We plot the inverse decay times as a function of V_{SD} for photon energies above (blue) and below (red) E_{22} . Similar to device 1 (Figure 6.4), both data sets extrapolate to a V_{SD} value consistent with the open circuit voltage $V_{OC} = 0.5$ V. However, while $1/\tau$ indeed scales linearly with V_{SD} , it exhibits a much steeper decent for $E_{PH} < E_{22}$. We fit both data sets and calculate the ratio of the extracted lifetimes and find $\tau_2 / \tau_1 \sim 1.7$, consistent with our hypothesis.

6.7 Double Pulse Photocurrent: Reverse Bias

Finally, we consider high reverse bias region of Figure 6.4. The escape time becomes shorter and approaches a constant value τ_0 . To understand this behavior, we can compare the

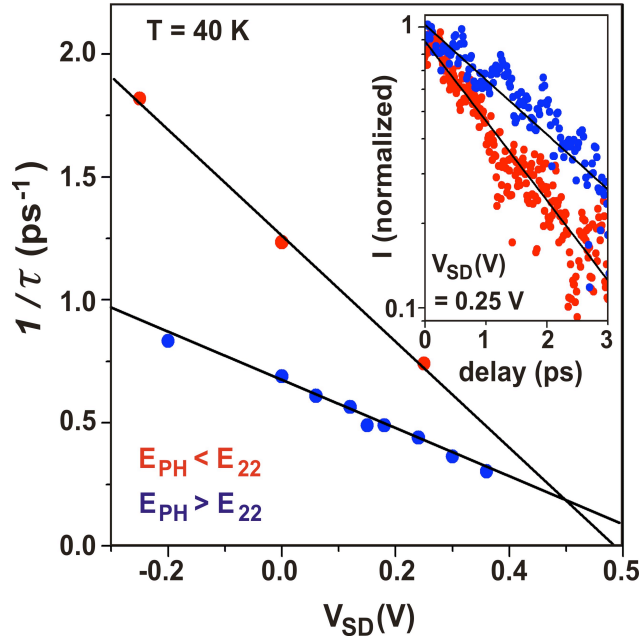


Figure 6.6. Double pulse photocurrent of the NT p-i-n photodiode as a function of photon energy. Inset, normalized photocurrent at $T = 40$ K vs. time delay at $E_{PHOTON} = 1.51$ eV (blue) and $E_{PHOTON} = 0.85$ eV (red) for device 2 with $V_{SD} = 0.25$ V. Device 2 has the same device geometry as device 1 with $V_1 = -10$ V, $V_2 = 10$ V, $V_G = 0.5$ V and $V_{OC} = 0.5$ V. **Main panel:** extracted inverse decay constants as a function of V_{SD} for $E_{PHOTON} = 1.51$ eV (blue) and $E_{PHOTON} = 0.85$ eV (red) with linear fits to the data.

escape time τ to the average time between scattering events τ_S . If the average time between scattering events $\tau_S = L_{MFP} / v_F$ is less than the escape time τ , then carriers undergo diffusive transport through the junction. This is observed in forward bias. However, if $\tau_S \geq \tau$, then carriers may escape the junction without scattering and the escape time approaches the ballistic limit. In this limit, the transit time for a ballistic carrier across half of the junction ($L \sim 0.5 \mu\text{m}$) would exhibit crossover behavior to a constant escape time $\tau_0 = L / v_F \sim 0.6 \text{ ps}$ at sufficiently high reverse bias. This crossover behavior is indeed observed (solid blue line Figure 6.4). However, the measured escape time is close to the experimental resolution of 0.4 ps, so further measurements with higher temporal resolution are needed to definitively confirm ballistic transport. Note that ballistic transport in reverse bias is consistent with previous findings in which E_{22} electrons and holes undergo highly efficient impact excitation resulting in multiple e-h pairs (Gabor et al. 2009, Wang et al. 2005, Baer et al. 2010).

6.8 Conclusion

In this Chapter, we have reported the first ultrafast photocurrent measurements that access the dynamics of electrons and holes in an individual nanotube p-i-n junction. These experiments open the door to future photocurrent studies exploring aspects of NT optoelectronic response that have previously been probed only through optical measurements, including electron-hole (exciton) recombination, phonon relaxation, and photoluminescence at various temperatures and photon energies. Additionally, increased temporal resolution may reveal dynamics of exciton dissociation that lead to free carriers on short time scales. Our technique will open the door for more detailed measurements of multiple electron-hole pair generation (Gabor et al. 2009, Wang et al. 2010, Schaller et al. 2004, Ellingson et al. 2005) and electron-hole recombination (Wang et al. 2004, Huang et al. 2006) in other individual nanoscale devices that incorporate nanotubes, graphene, semiconductor nanowires and nanocrystal quantum dots.

CHAPTER 7

CONCLUSION

7.1 The PN Junction Then and Now

In Chapter 1, we introduced the semiconductor PN junction and set out to explore the physics of a PN junction composed of a one-dimensional quantum wire. In our PN junction, the functional element was the carbon nanotube, an organic macromolecule with aspects of both semiconductor crystal and biological molecule. By wiring up the NT and studying optoelectronic transport, we revealed some of the wonders of this material. Indeed, we discovered that the NT operates as a one-dimensional wire (Chapter 4), and then went on to explore charge carrier interactions and dynamics in the NT. We first discovered extremely efficient generation of multiple electron-hole pairs (Chapter 5), which promises to dramatically improve solar energy harvesting. We then explored the dynamics and interactions of electrons and holes in real time (Chapter 6), and directly measured the escape of electrons and holes out of the PN junction.

In Chapter 1, Figure 1.2, we showed the original patent of the semiconductor PN junction by R.S. Ohl, a schematic of the electron potential energy and transport characteristics. In Figure 7.1, the final figure of this thesis, we summarize the interesting physics revealed in our nanotube PN junction. From these two figures, we can indeed compare and contrast the PN junction then and now. While it is interesting to see how the PN junction has changed in half a century, it is more interesting, and even awe-inspiring, to recognize the foresight of such great experimentalists as Ohl, without whom the work presented here may not exist.

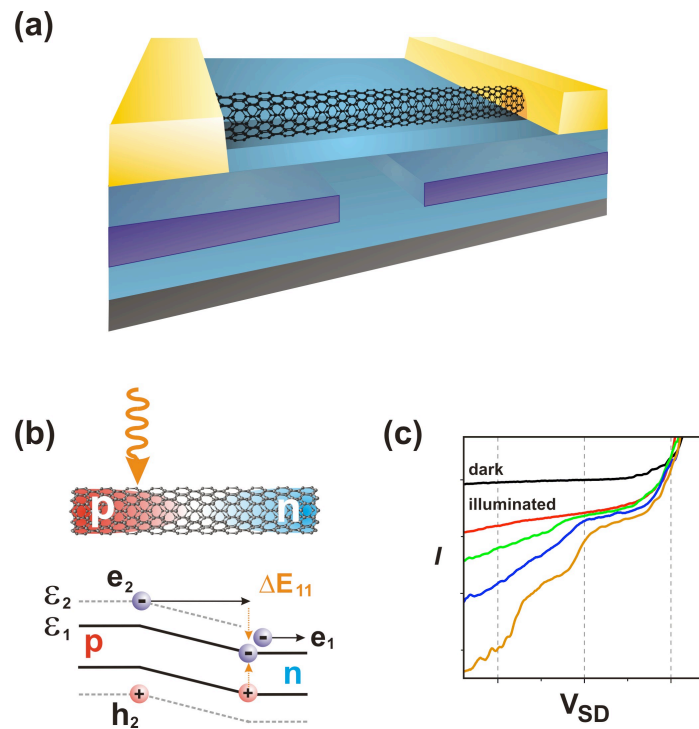


Figure 7.1. The carbon nanotube PN junction. **(a)** a schematic of the multiple gate nanotube PN junction. **(b)** Schematic potential energy diagram for electrons in the NT PN junction. An incident photon excites an electron-hole pair in the junction that undergoes efficient multiplication. **(c)** Current-voltage characteristics for the unconventional nanotube PN junction.

REFERENCES

- Ashcroft, N. W. and N. D. Mermin *Solid State Physics*.
Orlando, Saunders College (1976).
- Avouris, P. *Nano Letters* **10**, 4285 (2010).
- Avouris, P., et al. *Nature Nano* **2**, 605 (2007).
- Bachtold, A., et al. *Science* **294**, 1317 (2001).
- Baer, R. and E. Rabani, *Nano Letters* **10**, 3277 (2010).
- Berger, S., et al. *Nano Letters* **7**, 398 (2007).
- Birks, T. A., et al. *Optics Letters* **25**, 1415 (2000).
- Bockrath, M., et al. *Nature* **397**, 598 (1999).
- Bosnick, K., et al. *Applied Physics Letters* **89**, 163121 (2006).
- Capaz, R. B., et al. *Physical Review Letters* **94**, 036801 (2005).
- Chen, J., et al. *Science* **310**, 1171 (2005).
- Datta, S. *Electron Transport in Mesoscopic Systems*. Cambridge,
Cambridge University Press (1995).
- Dekker, C. *Physics Today* **52**, 22 (1999).
- Dresselhaus, M. S., G. Dresselhaus, et al., *Carbon Nanotubes*. Topics in
Applied Physics. New York, Springer (2001).
- Ellingson, R. J., et al. *Nano Letters* **5**, 865 (2005).
- Freitag, M., et al. *Nano Letters* **3**, 1067 (2003).
- Gabor, N. M., et al. *Science* **325**, 1367 (2009).
- Hagen, A., et al. *Physical Review Letters* **95**, 197401 (2005).

Hayden, O., et al. *Nature Materials* **5**, 352 (2006).

Hertel, T. and G. Moos. *Physical Review Letters* **84**, 5002 (2000).

Huang, L. and T. D. Krauss, *Physical Review Letters* **96**, 057407 (2006).

Ilani, S. and P. L. McEuen. *Annual Review of Condensed Matter Physics* **1**, 1 (2010).

Javey, A., et al. *Nature Materials* **1**, 241 (2002).

Javey, A., et al. *Nature* **424**, 654 (2003).

Javey, A., et al. *Physical Review Letters* **92**, 106804 (2004).

Jorio, A., G. Dresselhaus, M. S. Dresselhaus. *Carbon Nanotubes: Advanced Topics in Synthesis, Structures, Properties and Applications*. Berlin, Springer (2008).

Kane, C. L. and E. J. Mele. *Physical Review Letters* **90**, 207401 (2003).

Kane, C. L. and E. J. Mele. *Physical Review Letters* **93**, 197402 (2004).

Katsnelson, M. I., et al. *Nature Physics* **2**, 620 (2006).

Kim, J., et al. *Applied Physics Letters* **92**, 031107 (2008).

Kim, W., et al. *Nano Letters* **3**, 193 (2003).

Kinder, J. M., and E. J. Mele. *Physical Review B* **78**, 155429 (2008).

Kong, J., et al. *Nature* **395**, 878 (1998).

Kong, J., et al. *Science* **287**, 622 (2000).

Larrimore, L., et al. *Nano Letters* **6**, 1329 (2006).

Larrimore, L. *Chemical and Biological Sensing with Carbon Nanotubes in Solution*. Ithaca, Cornell University Ph.D. thesis (2007).

Lee, J. U., et al. *Applied Physics Letters* **85**, 145 (2004).

Lee, J. U. *Applied Physics Letters* **87**, 073101 (2005).

Lee, J. U., et al. *Applied Physics Letters* **90**, 053103 (2007).

Leonard, F. and J. Tersoff. *Physical Review Letters* **83**, 5174 (1999).

Li, J., et al. *Nano Letters* **3**, 597 (2003).

Liang, W., et al. *Nature* **411**, 665 (2001).

Liao, A., et al. *Physical Review Letters* **101**, 256804 (2008).

Lin, C. and R. H. Stolen. *Applied Physics Letters* **28**, 216 (1976).

Lu, C. G., et al. *Nano Letters* **4**, 623 (2004).

Ma, Y. -Z., et al. *Molecular Physics* **104**, 1179 (2006).

Mann, D., et al. *Nano Letters* **3**, 1541 (2003).

Manzoni, C., et al. *Physical Review Letters* **94**, 207401 (2005).

Marty, L., et al. *Physical Review Letters* **96**, 136803 (2006).

McClure, J. W. *Physical Review* **104**, 666 (1956).

McEuen, P. L. *Physics World* **13**, 31 (2000).

McEuen, P. L. *Nature* **393**, 15 (1998).

Minot, E. D., et al. *Physical Review Letters* **90**, 156401 (2003).

Minot, E. D., et al. *Nature* **428**, 536 (2004).

Minot, E. D. *Tuning the Band Structure of Carbon Nanotubes*. Ithaca,
Cornell University Ph.D. thesis (2004).

Misewich, J. A., et al. *Science* **300**, 783 (2003).

Novoselov, K. S., et al. *Nature* **438**, 197 (2005).

Odintsov, A. A. *Physical Review Letters* **85**, 150 (2000).

Ohl, R. S. *Light Sensitive Electric Device*. U.S. Patent 2,402,662 (1941).

Park, J. Y. et al. *Nano Letters* **4**, 517 (2004).

Perebeinos, V., et al. *Physical Review Letters* **94**, 086802 (2005).

Perebeinos, V., et al. *Physical Review B* **74**, 121410 (2006).

Ponomarenko, L. A., et al. *Science* **320**, 356 (2008).

Pop, E., et al. *Physical Review Letters* **95**, 155505 (2005).

Prechtel, L., et al. *Nano Letters* **11**, 269 (2011).

Rosenblatt, S., et al. *Nano Letters* **2**, 869 (2002).

Rosenblatt, S., et al. *Applied Physics Letters* **87**, 153111 (2005).

Rosenblatt, S. *Pushing the Limits of Carbon Nanotube Transistors*. Ithaca, Cornell University Ph.D. thesis (2005).

Saito, R., G. Dresselhaus and M. S. Dresselhaus. *Physical Properties of Carbon Nanotubes*. London, Imperial College Press (1998).

Schaller, R. D. and V. I. Klimov. *Physical Review Letters* **92**, 186601 (2004).

Schaller, R. D., et al. *Nature Physics* **1**, 189 (2005).

Shockley, W. and H. J. Queisser. *Journal of Applied Physics* **32**, 510 (1961).

Snow, E. S., et al. *Science* **307**, 1942 (2005).

Spataru, C. D., et al. *Physical Review Letters* **92**, 077402 (2004).

Sze, S. M. *Physics of Semiconductor Devices*. London, Wiley (1981).

Tans, S. J., M. H. Devoret, et al. *Nature* **394** 761 (1998).

Tian, B., et al. *Nature* **449**, 885 (2007).

Valkunas, L., et al. *Physical Review B* **73**, 115432 (2006).

van Hove, L. *Physical Review* **89**, 1189 (1953).

Van Wees, B. J. *Physical Review Letters* **60**, 848 (1998).

Wallace, P. R. *Physical Review* **71**, 622 (1947).

- Wang, F., et al. *Physical Review Letters* **92**, 177401 (2004).
- Wang, F., G. Dukovic, et al. *Science* **308**, 838 (2005).
- Wang, F., et al. *Physical Review B* **73**, 245424 (2006).
- Wang, S. et al. *Nano Letters* **10**, 2381 (2010).
- Weinberg, S. *The Quantum Theory of Fields: Modern Applications*.
Cambridge, Cambridge University Press (1995).
- Wharam, D. A., et al. *Journal of Physics C Solid State Physics*
21, 209 (1988).
- White, C. T. and J. W. Mintmire, *Nature* **394**, 29 (1998).
- Yang, C., et al. *Nano Letters* **6**, 2929 (2006).
- Yao, Z., et al. *Physical Review Letters* **84**, 2941 (2000).
- Zhou, C., et al. *Science* **290**, 1552 (2000).
- Zhou, X., et al. *Physical Review Letters* **95**, 146805 (2005).
- Zhou, X., et al. *Nature Nanotechnology* **2**, 185 (2007).
- Zhou, X. *Carbon Nanotube Transistors, Sensors, and Beyond*. Ithaca,
Cornell University Ph.D. thesis (2007).